Mechanical Systems and Signal Processing 117 (2019) 609–633

Contents lists available at ScienceDirect

Mechanical Systems and Signal Processing

journal homepage: www.elsevier.com/locate/ymssp

Tailoring concurrent shear and translational vibration control mechanisms in elastomeric metamaterials for cylindrical structures

Sih-Ling Yeh, Ryan L. Harne *

Department of Mechanical and Aerospace Engineering, The Ohio State University, Columbus, OH 43210, USA

ARTICLE INFO

Article history:
Received 10 May 2018
Received in revised form 23 July 2018
Accepted 26 July 2018

Keywords:
Metamaterials
Elastomers
Vibration control
Broadband frequency

ABSTRACT

The implementation of engineered metamaterials in practical engineering structures for vibration control purposes is challenged by a lack of understanding on the specific interaction mechanisms present among finite-sized metamaterials and the greater host structures. This research begins to address such knowledge gap by establishing an analytical framework to study the dynamic response and coupling mechanisms between elastomeric metamaterial inclusions embedded within a cylindrical host structure, representative of a variety of engineering systems. The analysis is formulated based on energy methods, and approximately solved by the Ritz method. Following experimental validation, the analysis is leveraged to reveal deep understanding on the precise mechanisms of coupling between such elastomeric metamaterial inclusions and the host structure. Several non-intuitive roles of parameter changes are conclusively revealed. For instance, while the decrease in open angle ratio of the inclusion cross-section geometry and the increase in the central core radius both appear to increase the significance of the core mass, the analysis reveals that the primary inclusion characteristic tuned by such parameter changes is the dynamic stiffness of the inclusions. Together, the dynamic mass and dynamic stiffness work to induce two tuned-mass-damper-like behaviors that lead to broadband vibration attenuation capabilities. The results of this research encourage attention to the study of specific problems whereby metamaterials directly interact with host structures to accurately understand the working mechanisms of vibration control for sake of optimal practical implementation.

1. Introduction

A long-standing demand remains for exceptional vibration attenuation in many engineering applications. Lightweight materials that deliver high vibration attenuation capabilities extend the life of engineering systems and improve working quality. With these aims in mind, previous researchers have investigated structural and material systems capable of attenuating broadband vibration by using the concepts of tuned mass dampers, bandgap behavior, and constrained layered dampers.

* Corresponding author.
E-mail address: harne.3@osu.edu (R.L. Harne).

https://doi.org/10.1016/j.ymssp.2018.07.049
0888-3270/

Tuned mass dampers (TMDs) are mass-spring-damper resonators capable of transferring the local vibration energy from the host structure to the mass-spring-damper. With this additional degree-of-freedom available, the vibration of the host structure may be suppressed by out-of-phase reaction force of the TMD with respect to the phase of the excitation force. Researchers have investigated tailoring this mechanism of vibration absorption via a variety of approaches. For example, Pai [1] proposed an elastic metamaterial with one-dimensional TMD subsystems to realize broadband vibration absorption for a one-dimensional host structure. The TMDs supply inertial forces that attenuate longitudinal wave propagation, including when the longitudinal wavelengths are much greater than the size of the periodic TMD subsystem, or unit cell. Similarly, Sun et al. [2] designed an elastic metamaterial beam with an array of TMD subsystems that exert shear forces and bending moments to absorb transverse wave propagation. Pai et al. [3] reported that using dual-mass TMD subsystems may enhance vibration absorption in two-dimensional structures while also broadening the range of frequencies of wave attenuation. Nonetheless, for each TMD the attenuation is only effective for a relatively narrow frequency range of resonance inherent to the TMDs or array of TMDs.

In a similar spirit to the resonant behavior of TMDs, bandgaps are a promising property of metamaterials for vibration absorption since waves are prohibited from propagating through the host structure at frequencies within the bandgap. The center frequency, bandwidth, and number of the bandgaps are related to the interrelationships among geometry, stiffness, and filling fraction of the metamaterials within the media. For example, Wang et al. [4] reported that the number of bandgaps increases as the metamaterial is subjected to increasing compressive strain while the center frequency and bandwidth simultaneously reduce. With the aim to combine local resonance and bandgap behaviors, Matlack et al. [5] adopted resonant elements embedded in a polycarbonate lattice to realize a broad Bragg bandgap. The bandgap breadth and center frequency were thus shown to be controlled by the local resonances. Indeed, the breadth of metamaterial concepts that exhibit bandgap behaviors are diverse and are inspiring for new approaches via their combination. For instance, Nouh et al. [6] presented a metamaterial plate composed of periodic cells with a small mass on a viscoelastic membrane, while Oh et al. [7] developed an elastic metamaterial insulator capable of creating a broad bandgap at low frequency by combined shear stiffening and rotation softening. Furthermore, for the chiral elastic metamaterial inclusions, Liu et al. [8] and Zhu et al. [9] investigated chiral metamaterials with inclusions comprised of a core with coating layer. Also using a multi-material concept, Baravelli and Ruzzene [10] found that reduction of the filling fraction of the periodic elements caused the number of bandgaps to increase and the center frequency to decrease. Abdeljaber et al. [11] reported that the use of segmented, non-continuous, and non-periodic metamaterials may be advantageous for vibration and wave control in engineering structures. Although locally resonant bandgap mechanisms may provide useful means to suppress target bandwidths of elastic waves in host structures, the bandwidth effected by such phenomena may be limited. Such limitation is inevitable when utilizing a parameter sensitive resonant behavior. Furthermore, designing these metamaterials to attenuate low frequency waves requires large size and often more material mass, which are undesirable aspects in practice.

Constrained layer damping (CLD) materials introduce an alternative strategy for vibration attenuation and typically use small added mass. The attenuation mechanism of CLD is attributed to the shear deformation in the thin and soft viscoelastic layer between the host structure and the constraining layer. As a result, CLD provides vibration control most effectively at wavelengths on the order or shorter than the size of the applied CLD materials. This bounds the effective working range of the CLD to mid to high frequencies in practical applications. Using these principles, Aumjaud [12] developed a double shear lap-joint damper to yield high modal loss factor and amplitude reduction for a minimum of added mass. Additionally, previous researchers discussed influences of the length, elastic modulus, thickness, structural damping, and interfacial damping of the viscoelastic layer that is central to the CLD approach [13–20]. Douglas and Yang [21] concluded that the thin viscoelastic material provides broadband vibration attention by way of enhanced shear transfer to the viscoelastic layer, which agrees with findings by Kerwin [22]. For thicker viscoelastic layers, the broadband attenuation of vibration is less apparent whereas transverse compressional damping phenomena may occur. Although conventional CLD may provide broadband attenuation at mid to high frequencies, the CLD must cover a large proportion of the host structure, which is challenging in practice and may have side-effects, such as introducing a thermally insulating layer.

The survey above identifies promise and shortcomings for the variety of techniques for vibration attenuation: TMD, bandgap, and CLD. Recent work has sought to advance beyond these techniques by utilizing compression constraint on lightweight, elastomeric metamaterials. In this spirit, Bishop et al. [23] reported a lightweight hyperdamping metamaterial inclusion capable of attenuating more impact energy than the bulk material from which the metamaterial was derived. The concept was extended by Harne et al. [24] who utilized such inclusions to enhance noise control capabilities of poroelastic media. Yet, to date, the working mechanisms by which metamaterials enhancing vibration attenuation in host structures has not been illuminated. Consequently, this research aims to build up an analytical framework to study the lightweight metamaterial inclusions, originally proposed in [23,24], as the inclusions interact with a host structure.

The metamaterial inclusions considered here are cylindrical so as to conform for a host structure that is a circular hollow tubular beam, a common component in automotive and aerospace structures as well as in mechanical equipment. The bottom left image of Fig. 1(a) illustrates the concept, where an elastomeric inclusion is embedded within a greater host structure (e.g. a long cylindrical tube). Several components to the cross-section may be identified using the general schematic at the top of Fig. 1(a) shown by the four distinct layers. In Fig. 1(b), the annular metamaterial layer (labeled 2 in Fig. 1(a)) is the thin outer-most component of the metamaterial that is between the host structure (labeled 1) and the porous metamaterial layer (labeled 3). The core bulk metamaterial layer (labeled 4) at the center of the metamaterial is a mass. All together, the radially arrayed beams are analogous to a soft elastic layer.

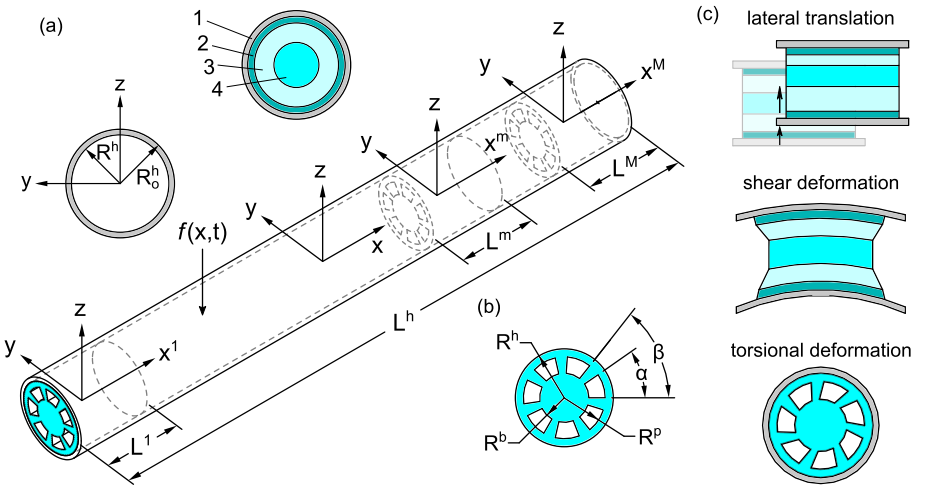

Fig. 1. (a) Schematic of host beam and beam with metamaterial inclusion. (b) Schematic of cross-section dimensions of metamaterial inclusion. (c) Three different deformations in the analytical model. (d) Photograph of experimental setup.

The porous and core bulk metamaterial layers may be similar to a TMD for metamaterial deformation that is due to transverse up/down motion of the core, as schematically shown in Fig. 1(c) via the lateral translation mechanism. In addition, the shorter wavelength bending of the host structure deforms the metamaterial inclusion in shear, Fig. 1(c). Since the radially arrayed beams of the porous metamaterial layer are soft in comparison to the solid core, a CLD-like shear damping is anticipated at mid to high frequencies of vibration. Finally, the lowest order motion of the constrained inclusions is known to be rotation [24]. As a result, a third mode of action of the inclusion against the host structure exists via the relation rotation of the metamaterial inclusion core with respect to the rotation of the host structure. By exploiting these multiple mechanisms of vibration attenuation, a more versatile capability to suppress broadband frequency vibrations may be realized, while concurrently minimizing added mass via the cellular void architecture of the inclusions and need for few inclusions if the many attenuation mechanisms are fully harnessed.

To understand the interactions between the host tube structure and the metamaterial inclusion and to clarify the full opportunities for broadband vibration attenuation, this study devises, validates, and then leverages an analytical model for the vibration response of the host tube structure with metamaterial inclusions. This report undertakes and details the following efforts in this research. The analytical model formulation is first described, wherein lateral translation, shear deformation, and torsional deformation that couple the inclusions to the host via the radially arrayed beams are taken into account. Euler-Lagrange equations are used to derive the governing equations of motion for the response when the host structure is harmonically forced. The solution technique utilized to approximately solve the equations is the Ritz method and trigonometric functions [25] are employed for the trial functions in the Ritz expansion [26]. To verify the analytical model, experiments are undertaken and the data is rigorously discussed in relation to the analytical predictions. The analytical model is then leveraged to investigate the dynamic interaction mechanisms between the host structure and inclusions that may give rise to exceptional vibration attenuation capabilities. A final section concludes this work with a consolidation of principal discoveries.

2. Overview of host structure and metamaterial inclusions

The host structure considered in this work is a cylindrical, tubular beam shown in Fig. 1(a). The tubular beam of length L, outer radius R^h_o, and inner radius R^h is examined with free-free boundary conditions. This host structure is composed from an elastic material with complex Young's modulus E^h, density ρ^h, structural loss factor η^h, mass-proportional damping coefficient α^h, and stiffness-proportional damping coefficient β^h. The superscript h indicates a host structure relevant parameter. The beam is excited by a number P of lateral harmonic point forces $f(x,t)$, which are applied on the surface of the beam in the z axis as shown in Fig. 1(a).

A number M of metamaterials of length L^m are embedded in the host structure. For the sake of simplicity, each embedded metamaterial is assumed to be composed from the same viscoelastic material and thus have the same properties as the other metamaterial inclusions. The superscript m indicates a metamaterial relevant parameter: E^m is Young's modulus, ν^m is Poisson's ratio, ρ^m is density, η^m is structural loss factor, α^m is mass-proportional damping coefficient, and β^m is stiffness-proportional damping coefficient. The use of multiple means for damping in the analytical framework is based on experimental results that suggest several mechanisms for energy dissipation are present. Here, the study adopts hysteretic

damping and Rayleigh damping. The damping coefficients are identified empirically, which is the commonly adopted technique [27,28].

To account for the exact geometry of the system including the voids in the metamaterial inclusion, the host structure with metamaterial inclusion is considered to be composed of four unique layers as shown in Fig. 1(a). In the model formulation, the exact geometries of the cross-sections are accounted for, whereas the schematic in the top of Fig. 1(a) is for illustrative purposes only. The layer 1 is the host structure with radius $R^h < r < R_o^h$. The layer 2 is the thin annular metamaterial layer, which is a solid material of radius $R^p < r < R^h$. The layer 3 is the porous metamaterial layer composed of radially arrayed beams with radius $R^b < r < R^p$. Finally, the layer 4 is a core bulk metamaterial layer with radius $0 < r < R^b$. The annular metamaterial layer is practically required to support the radially arrayed beams. The layers 1–4 shown in Fig. 1(a) are for visualization purposes only since the exact geometries are utilized in the model formulation as described in Section 3.

3. Analytical model formulation

The analytical modeling approach accounts for realistic elastic and dissipation coupling mechanisms between the host structure and metamaterial inclusions. This Section 3 provides an overview of the model formulation. First, the deformations of each layer are identified. Then, the kinetic and potential energies for each layer are obtained. By adopting assumed solutions based on the Ritz method, the Euler-Lagrange governing equations for the coupled system are solved.

3.1. Deformations and energies

For the host beam structure layer, labeled 1 in Fig. 1(a), only translational displacement is considered since excitations to the host beam occur perpendicular to the axis of the beam. The host structure translational displacement w^h is dependent on the x coordinate and time t, $w^h = w^h(x,t)$. Shear and torsional deformations do not result because the host structure is long and slender, and torsional deformation is not induced by the lateral force excitations. In a cylindrical coordinate system (r,θ,x), the host structure exists from $R^h < r < R_o^h$, $0 < \theta < 2\pi$, and $0 < x < L$. Expressed in the host Cartesian coordinate system (x, y, z), with origin at the center of the host tube, one obtains a set of deformations given by

$$u_x^h = -zw_{,x}^h \tag{1a}$$

$$u_y^h = 0 \tag{1b}$$

$$u_z^h = w^h \tag{1c}$$

The subscript $(\,)_{,x}$ indicates a partial derivative of the function with respect to the x coordinate.

The core bulk metamaterial at the center of the inclusion is a non-slender beam. As a result, Timoshenko beam theory is adopted to characterize the relative influences of bending and shear deformation in the core layer. In addition to the lateral translation and shear deformation induced by bending deformation, the torsional deformation is taken into account. The bulk metamaterial lateral displacement $w^b = w^b(x^m,t)$, shear angle $\psi^b = \psi^b(x^m,t)$ in the $x^m z$ plane, torsional angle $\alpha^b = \alpha^b(x^m,t)$ in the yz plane are functions of the x^m coordinate, whose origin is at the center of the inclusion, and time t. The superscript b refers to the core bulk metamaterial layer. The displacements of the bulk metamaterial layer $(0 < r < R^b,\ 0 < \theta < 2\pi)$ in the metamaterial coordinate system (x^m, y, z) are

$$u_x^b = -z\psi^b \tag{2a}$$

$$u_y^b = -z\alpha^b \tag{2b}$$

$$u_z^b = w^b + y\alpha^b \tag{2c}$$

The interfacial surfaces are assumed to maintain perfect contact between adjacent layers, so that translational, shear, and torsional deformations are continuous between adjacent layers. The deformations with the metamaterial inclusion annular and porous layers are thus associated with the relative motions between the host structure and the core bulk metamaterial layer. The thin annular metamaterial layer is bound by the host beam and porous metamaterial layer. There is no torsional deformation of the host tubular beam and the annular metamaterial layer is thin, so torsional deformation is neglected in the thin annular metamaterial layer. As a result, the displacements of the annular metamaterial layer are assumed to be functions of the displacements of the core metamaterial and the host tubular beam. The annular metamaterial lateral displacement $w^a = w^a(x^m,y,z,t)$ and shear angle $\psi^a = \psi^a(x^m,y,z,t)$ in the $x^m z$ plane are linearly distributed along the radial direction (r-coordinate) from the host tube to the core metamaterial. The superscript a refers to the annular metamaterial layer. The displacements of the annular metamaterial layer $(R^p < r < R^h,\ 0 < \theta < 2\pi)$ in the metamaterial coordinate system (x^m, y, z) are

$$u_x^a = -z\psi^a \tag{3a}$$

$$u_y^a = 0 \tag{3b}$$

$$u_z^a = w^a \tag{3c}$$

where $w^a = \frac{r-R^b}{R^h-R^b}w^h + \frac{R^h-r}{R^h-R^b}w^b$ and $\psi^a = \frac{r-R^b}{R^h-R^b}w^h_{,x} + \frac{R^h-r}{R^h-R^b}\psi^b$.

The voids in the porous metamaterial layer introduce much greater macroscopic softness to the porous layer than the stiffnesses present for the host structure, annular metamaterial layer, and bulk metamaterial layer. Consequently, in this research the porous metamaterial layer is assumed to undergo lateral translation, shear, and torsional deformations caused by the relative deformations between the host structure and the bulk metamaterial layer. In addition, the exact cross-section geometry of the radially arrayed beams is accounted for to enhance the fidelity of the predicted contributions of each form of deformation (i.e. translation, shear, torsion). Similar to the annular metamaterial layer, the porous metamaterial lateral displacement $w^p = w^p(x^m, y, z, t)$, shear angle $\psi^p = \psi^p(x^m, y, z, t)$ in the $x^m z$ plane, and torsional angle $\alpha^p = \alpha^p(x^m, y, z, t)$ in the yz plane are linearly distributed along the radial direction (r-coordinate) from the host beam to the core metamaterial. The superscript p refers to the porous metamaterial layer. The displacements of each radially arrayed beam ($R^b < r < R^p$, $\theta_{1n} < \theta < \theta_{2n}$, $\theta_{1n} = \alpha + (n-1)\beta$, $\theta_{2n} = n\beta$, $n = 1, 2, .., N$, and N is the amount of radially arrayed beams) in the metamaterial coordinate system (x^m, y, z) are

$$u_x^p = -z\psi^p \tag{4a}$$

$$u_y^p = -z\alpha^p \tag{4b}$$

$$u_z^p = w^p + y\alpha^p \tag{4c}$$

where $w^p = \frac{r-R^b}{R^h-R^b}w^h + \frac{R^h-r}{R^h-R^b}w^b$, $\psi^p = \frac{r-R^b}{R^h-R^b}w^h_{,x} + \frac{R^h-r}{R^h-R^b}\psi^b$, and $\alpha^p = \frac{R^h-r}{R^h-R^b}\alpha^b$. The w^a, ψ^a, w^p, ψ^p, and α^p are determined according to continuity of deformation from one layer to the next.

Consequently, based on the deformation profiles defined in Eqs. (1)–(4), the unique deformations in the system are the host lateral translation w^h, the bulk metamaterial lateral translation w^b, the bulk metamaterial shear angle ψ^b, and the bulk metamaterial torsional rotation α^b.

Normalization is applied in order to utilize the desired trial functions for the application of the Ritz method. The axial coordinates of the host tube x and each metamaterial inclusion x^m are normalized by

$$\xi = \frac{2x}{L}, \quad \xi^m = \frac{2x^m}{L^m} \tag{5}$$

The relationship between the normalized coordinate of the host ξ and each metamaterial ξ^m is

$$\xi = \xi_m + \frac{L^m}{L^h}\xi^m \tag{6}$$

where the ξ_m is the center of the metamaterial inclusion in the ξ-coordinate (normalized host coordinate).

Based on the deformations of each layer, the velocities and strains are then evaluated. The kinetic and potential energies of each layer are subsequently determined. The length integrals of the energies are transformed using the normalized coordinates Eq. (5). The kinetic energies of the host layer T^h, the annular metamaterial layer T^a, the porous metamaterial layer T^p, and the core bulk metamaterial layer T^b are respectively given in Eqs. (7a)–(7d). The subscript $(\,)_{,t}$ indicates partial differentiation with respect to time t and multiple subscripts indicate combined partial derivatives, e.g. $(\,)_{,\xi t} = \partial^2(\,)/\partial\xi\partial t$.

$$T^h = \frac{\rho^h A^h L}{4}\int_{-1}^{1}\left(w^h_{,t}\right)^2 d\xi + \frac{\rho^h I^h}{L}\int_{-1}^{1}\left(w^h_{,\xi t}\right)^2 d\xi \tag{7a}$$

$$\begin{aligned} T^a = {} & \frac{\rho^m I^a_{10}}{L^m}\int_{-1}^{1}\left(w^h_{,\xi^m t}\right)^2 d\xi^m + \frac{\rho^m A^a_{30} L^m}{4}\int_{-1}^{1}\left(w^h_{,t}\right)^2 d\xi^m + \frac{\rho^m A^a_{31} L^m}{4}\int_{-1}^{1}\left(w^b_{,t}\right)^2 d\xi^m \\ & + \frac{\rho^m I^a_{12} L^m}{4}\int_{-1}^{1}\left(\psi^b_{,t}\right)^2 d\xi^m + \frac{\rho^m A^a_{34} L^m}{4}\int_{-1}^{1} w^h_{,t} w^b_{,t} d\xi^m + \frac{\rho^m I^a_{15}}{2}\int_{-1}^{1} w^h_{,\xi^m t}\psi^b_{,t} d\xi^m \end{aligned} \tag{7b}$$

$$\begin{aligned} T^p = {} & \frac{\rho^m I^p_{10}}{L^m}\int_{-1}^{1}\left(w^h_{,\xi^m t}\right)^2 d\xi^m + \frac{\rho^m A^p_{30} L^m}{4}\int_{-1}^{1}\left(w^h_{,t}\right)^2 d\xi^m + \frac{\rho^m A^p_{31} L^m}{4}\int_{-1}^{1}\left(w^b_{,t}\right)^2 d\xi^m \\ & + \frac{\rho^m I^p_{12} L^m}{4}\int_{-1}^{1}\left(\psi^b_{,t}\right)^2 d\xi^m + \frac{\rho^m \left(I^p_{23}+I^p_{33}\right) L^m}{4}\int_{-1}^{1}\left(\alpha^b_{,t}\right)^2 d\xi^m \\ & + \frac{\rho^m A^p_{34} L^m}{4}\int_{-1}^{1} w^h_{,t} w^b_{,t} d\xi^m + \frac{\rho^m I^p_{15}}{2}\int_{-1}^{1} w^h_{,\xi^m t}\psi^b_{,t} d\xi^m + \frac{\rho^m \left(I^p_{36}+I^p_{38}\right) L^m}{4}\int_{-1}^{1} w^b_{,t}\alpha^b_{,t} d\xi^m \end{aligned} \tag{7c}$$

$$T^b = \frac{\rho^m A_{31}^b L^m}{4}\int_{-1}^{1}\left(w_{,t}^b\right)^2 d\xi^m + \frac{\rho^m I_{12}^b L^m}{4}\int_{-1}^{1}\left(\psi_{,t}^b\right)^2 d\xi^m + \frac{\rho^m\left(I_{23}^b + I_{33}^b\right)L^m}{4}\int_{-1}^{1}\left(\alpha_{,t}^b\right)^2 d\xi^m \tag{7d}$$

The expressions for the undefined coefficients of each layer in Eq. (7) are given in Appendix A. The potential energies of the host layer U^h, the annular metamaterial layer U^a, the porous metamaterial layer U^p, and the core bulk metamaterial layer U^b are respectively presented in Eqs. (8a)–(8d).

$$U^h = \frac{4\tilde{E}^h I^h}{L^3}\int_{-1}^{1}\left(w_{,\xi\xi}^h\right)^2 d\xi \tag{8a}$$

$$\begin{aligned}
U^a = {} & \frac{4\tilde{E}^m I_{10}^a}{\left(L^m\right)^3}\int_{-1}^{1}\left(w_{,\xi^m\xi^m}^h\right)^2 d\xi^m + \frac{\tilde{G}^m k^a\left(A_{50}^a + A_{60}^a\right)}{L^m}\int_{-1}^{1}\left(w_{,\xi^m}^h\right)^2 d\xi^m \\
& + \frac{\left(\tilde{E}^m I_{30}^a + \tilde{G}^m k^a J_{40}^a\right)L^m}{4}\int_{-1}^{1}\left(w^h\right)^2 d\xi^m \\
& + \frac{\tilde{G}^m k^a A_{51}^a}{L^m}\int_{-1}^{1}\left(w_{,\xi^m}^b\right)^2 d\xi^m + \frac{\left(\tilde{E}^m I_{31}^a + \tilde{G}^m k^a J_{41}^a\right)L^m}{4}\int_{-1}^{1}\left(w^b\right)^2 d\xi^m \\
& + \frac{\tilde{E}^m I_{12}^a}{L^m}\int_{-1}^{1}\left(\psi_{,\xi^m}^b\right)^2 d\xi^m + \frac{\tilde{G}^m k^a\left(A_{52}^a + A_{62}^a\right)L^m}{4}\int_{-1}^{1}\left(\psi^b\right)^2 d\xi^m \\
& - \frac{\tilde{G}^m k^a A_{54}^a}{L^m}\int_{-1}^{1} w_{,\xi^m}^h w_{,\xi^m}^b d\xi^m - \frac{\left(\tilde{E}^m I_{34}^a + \tilde{G}^m k^a J_{44}^a\right)L^m}{4}\int_{-1}^{1} w^h w^b d\xi^m \\
& + \frac{2\tilde{E}^m I_{15}^a}{\left(L^m\right)^2}\int_{-1}^{1} w_{,\xi^m\xi^m}^h \psi_{,\xi^m}^b d\xi^m - \frac{\tilde{G}^m k^a\left(A_{55}^a + A_{65}^a\right)}{2}\int_{-1}^{1} w_{,\xi^m}^h \psi^b d\xi^m + \frac{\tilde{G}^m k^a A_{57}^a}{2}\int_{-1}^{1} w_{,\xi^m}^b \psi^b d\xi^m
\end{aligned} \tag{8b}$$

$$\begin{aligned}
U^p = {} & \frac{4\tilde{E}^m I_{10}^p}{\left(L^m\right)^3}\int_{-1}^{1}\left(w_{,\xi^m\xi^m}^h\right)^2 d\xi^m + \frac{\tilde{G}^m k^p\left(A_{50}^p + A_{60}^p\right)}{L^m}\int_{-1}^{1}\left(w_{,\xi^m}^h\right)^2 d\xi^m \\
& + \frac{\left(\tilde{E}^m I_{30}^p + \tilde{G}^m k^p J_{40}^p\right)L^m}{4}\int_{-1}^{1}\left(w^h\right)^2 d\xi^m \\
& + \frac{\tilde{G}^m k^p A_{51}^p}{L^m}\int_{-1}^{1}\left(w_{,\xi^m}^b\right)^2 d\xi^m + \frac{\left(\tilde{E}^m I_{31}^p + \tilde{G}^m k^p J_{41}^p\right)L^m}{4}\int_{-1}^{1}\left(w^b\right)^2 d\xi^m \\
& + \frac{\tilde{E}^m I_{12}^p}{L^m}\int_{-1}^{1}\left(\psi_{,\xi^m}^b\right)^2 d\xi^m + \frac{\tilde{G}^m k^p\left(A_{52}^p + A_{62}^p\right)L^m}{4}\int_{-1}^{1}\left(\psi^b\right)^2 d\xi^m \\
& + \frac{\tilde{G}^m k^p\left(J_{53}^p + J_{63}^p\right)}{L^m}\int_{-1}^{1}\left(\alpha_{,\xi^m}^b\right)^2 d\xi^m + \frac{\left(\tilde{E}^m A_{23}^p + \tilde{E}^m A_{33}^p + \tilde{G}^m k^p A_{43}^p\right)L^m}{4}\int_{-1}^{1}\left(\alpha^b\right)^2 d\xi^m \\
& - \frac{\tilde{G}^m k^p A_{54}^p}{L^m}\int_{-1}^{1} w_{,\xi^m}^h w_{,\xi^m}^b d\xi^m - \frac{\left(\tilde{E}^m J_{34}^p + \tilde{G}^m k^p J_{44}^p\right)L^m}{4}\int_{-1}^{1} w^h w^b d\xi^m \\
& + \frac{2\tilde{E}^m I_{15}^p}{\left(L^m\right)^2}\int_{-1}^{1} w_{,\xi^m\xi^m}^h \psi_{,\xi^m}^b d\xi^m - \frac{\tilde{G}^m k^p\left(A_{55}^p + A_{65}^p\right)}{2}\int_{-1}^{1} w_{,\xi^m}^h \psi^b d\xi^m \\
& - \frac{\tilde{G}^m k^p\left(J_{56}^p - J_{66}^p\right)}{L^m}\int_{-1}^{1} w_{,\xi^m}^h \alpha_{,\xi^m}^b d\xi^m - \frac{\left(\tilde{E}^m J_{36}^p - \tilde{G}^m k^p J_{46}^p\right)L^m}{4}\int_{-1}^{1} w^h \alpha^b d\xi^m \\
& + \frac{\tilde{G}^m k^p A_{57}^p}{2}\int_{-1}^{1} w_{,\xi^m}^b \psi^b d\xi^m + \frac{\tilde{G}^m k^p J_{58}^p}{L^m}\int_{-1}^{1} w_{,\xi^m}^b \alpha_{,\xi^m}^b d\xi^m \\
& + \frac{\left(\tilde{E}^m J_{38}^p - \tilde{G}^m k^p J_{48}^p\right)L^m}{4}\int_{-1}^{1} w^h \alpha^b d\xi^m - \frac{\tilde{G}^m k^p\left(J_{69}^p - J_{59}^p\right)}{2}\int_{-1}^{1} \psi^b \alpha_{,\xi^m}^b d\xi^m
\end{aligned} \tag{8c}$$

$$U^b = \frac{\tilde{G}^m k^b A_{51}^b}{L^m}\int_{-1}^{1}\left(w^b_{,\xi^m}\right)^2 d\xi^m + \frac{\tilde{E}^m I_{12}^b}{L^m}\int_{-1}^{1}\left(\psi^b_{,\xi^m}\right)^2 d\xi^m + \frac{\tilde{G}^m k^b A_{52}^b L^m}{4}\int_{-1}^{1}\left(\psi^b\right)^2 d\xi^m + \frac{\tilde{G}^m k^b\left(J_{53}^b + J_{63}^b\right)}{L^m}\int_{-1}^{1}\left(\alpha^b_{,\xi^m}\right)^2 d\xi^m - \frac{\tilde{G}^m k^b A_{57}^b}{2}\int_{-1}^{1}\psi^b w^b_{,\xi^m} d\xi^m \tag{8d}$$

Here, $\tilde{E}^h = E^h(1+j\eta^h)$ and $\tilde{E}^m = E^m(1+j\eta^m)$ are the complex Young's modulus of the host beam and the metamaterial, respectively. The $\tilde{G}^m = \tilde{E}^m/[2(1+\nu^m)]$ is the complex shear modulus of the metamaterial. The $k^a = 2(1+\nu^m)/(4+3\nu^m)$, $k^p = 10(1+\nu^m)/(12+11\nu^m)$, and $k^b = 6(1+\nu^m)/(7+6\nu^m)$ are the shear coefficients in Timoshenko's beam theory for the annular metamaterial layer, porous metamaterial layer, and the bulk metamaterial layer, respectively. The formulas of the shear coefficients are derived by Cowper [29] in accordance with the unique cross-section geometries of each layer. The expressions for the coefficients in Eq. (8) are provided in Appendix A. The work W^b of the applied lateral force per unit length in the ξ-coordinate, $f(\xi,t)$, is given by

$$W^b = \frac{L}{2}\int_{-1}^{1} w^h f(\xi,t) d\xi \tag{9}$$

3.2. Euler-Lagrange governing equations and Ritz method solution approach

The Ritz method is employed to approximately solve the Euler-Lagrange governing equations for the system. A set of trigonometric functions $\phi_k(\eta)$ created by Beslin and Nicolas [25] is employed as the trial functions in the Ritz method expansion. The utility and computational efficiency of the trigonometric functions have been extensively assessed by Dozio [26]. The trigonometric functions $\phi_k(\eta)$ used as the trial functions in this work are

$$\phi_k(\eta) = \sin(a_k\eta + b_k)\sin(c_k\eta + d_k) \tag{10}$$

The coefficients a_k, b_k, c_k, and d_k are listed in Table 1. The selection of trial functions among the full trigonometric function set are determined by the boundary conditions. The analysis of the free-free host beam lateral displacement w^h and of the free-free core bulk metamaterial inclusion lateral displacement w^b retain all of the trigonometric functions of the set. The functions $\phi_2(\eta)$ and $\phi_4(\eta)$ are removed from the sequences utilized to account for the shear angle ψ^b and torsional angle α^b of the core bulk metamaterial layer based on the boundary conditions. The host lateral displacement w^h, core bulk metamaterial lateral displacement w^b, shear angle ψ^b, and torsional angle α^b are

$$\begin{aligned} w^h(\xi,t) &= a_f^{hb}(t)\phi_f^{hb}(\xi) \\ w^b(\xi^m,t) &= b_g^{mb}(t)\phi_g^{mb}(\xi^m) \\ \psi^b(\xi^m,t) &= c_h^{ms}(t)\phi_h^{ms}(\xi^m) \\ \alpha^b(\xi^m,t) &= d_i^{mt}(t)\phi_i^{mt}(\xi^m) \end{aligned} \tag{11a-d}$$

where a_f^{hb}, b_g^{mb}, c_h^{ms}, and d_i^{mt} are unknown generalized coordinates [30] to be determined, and ϕ_f^{hb}, ϕ_g^{mb}, ϕ_h^{ms}, and ϕ_i^{mt} are trial functions defined according to Eq. (10), where η is replaced by ξ or ξ^m, and k is replaced by f, g, h, or i. The superscripts *hb*, *mb*, *ms*, and *mt* refer to the following. The *hb* refers to host lateral displacement induced by bending, *mb* refers to metamaterial lateral displacement induced by bending, *ms* refers to metamaterial shear displacement induced by bending, and *mt* refers to metamaterial torsional displacement.

The Lagrangian functional of the coupled system is

$$L = T^h + T^a + T^p + T^b - \left(U^h + U^a + U^p + U^b\right) + W^b \tag{12}$$

The Euler-Lagrange governing equations for the system are

Table 1
Coefficients of trigonometric functions set.

k	a_k	b_k	c_k	d_k
1	$\pi/4$	$3\pi/4$	$\pi/4$	$3\pi/4$
2	$\pi/4$	$3\pi/4$	$-\pi/2$	$-3\pi/2$
3	$\pi/4$	$-3\pi/4$	$\pi/4$	$-3\pi/4$
4	$\pi/4$	$-3\pi/4$	$\pi/2$	$-3\pi/2$
>4	$\pi(k-4)/2$	$\pi(k-4)/2$	$\pi/2$	$\pi/2$

$$\frac{d}{dt}\left(\frac{\partial L}{\partial \dot{a}_f^{hb}}\right) - \frac{\partial L}{\partial a_f^{hb}} = 0 \tag{13a}$$

$$\frac{d}{dt}\left(\frac{\partial L}{\partial \dot{b}_g^{mb}}\right) - \frac{\partial L}{\partial b_g^{mb}} = 0 \tag{13b}$$

$$\frac{d}{dt}\left(\frac{\partial L}{\partial \dot{c}_h^{ms}}\right) - \frac{\partial L}{\partial c_h^{ms}} = 0 \tag{13c}$$

$$\frac{d}{dt}\left(\frac{\partial L}{\partial \dot{d}_i^{mt}}\right) - \frac{\partial L}{\partial d_i^{mt}} = 0 \tag{13d}$$

The time-dependent governing equations assume steady-state time-harmonic responses. As a result, the unknown generalized coordinates and the lateral force applied on the host structure exhibit time dependence of the form

$$a_f^{hb} = A_f^{hb} e^{j\omega t}, \quad b_g^{mb} = B_g^{mb} e^{j\omega t}, \quad c_h^{ms} = C_h^{ms} e^{j\omega t}, \quad d_i^{mt} = D_i^{mt} e^{j\omega t}, \quad f = F_f^{hb} e^{j\omega t} \tag{14a-e}$$

Substituting Eq. (14) into Eq. (13), the governing equations in the matrix form is

$$\left(-\omega^2[M] + j\omega[C] + [K]\right)\{q\} = \{F\} \tag{15}$$

where the mass matrix $[M]$, stiffness matrix $[K]$, unknown constants $\{q\}$, and forcing vector $\{F\}$ are Eq. (16)–(19), respectively.

$$[M] = \begin{bmatrix} M_{fp}^{hbhb} & M_{fq}^{hb1b} & M_{fr}^{hb1s} & M_{fs}^{hb1t} & \cdots & M_{fq}^{hbmb} & M_{fr}^{hbms} & M_{fs}^{hbmt} \\ & M_{gq}^{1b1b} & M_{gr}^{1b1s} & M_{gs}^{1b1t} & 0 & 0 & 0 & 0 \\ & & M_{hr}^{1s1s} & M_{hs}^{1s1t} & \vdots & \vdots & \vdots & \vdots \\ & & & M_{is}^{1t1t} & 0 & \vdots & \vdots & \vdots \\ & & & & \ddots & 0 & 0 & 0 \\ & & & & & M_{gq}^{mbmb} & M_{gr}^{mbms} & M_{gs}^{mbmt} \\ & \text{sym} & & & & & M_{hr}^{msms} & M_{hs}^{msmt} \\ & & & & & & & M_{is}^{mtmt} \end{bmatrix} \tag{16}$$

$$[K] = \begin{bmatrix} K_{fp}^{hbhb} & K_{fq}^{hb1b} & K_{fr}^{hb1s} & K_{fs}^{hb1t} & \cdots & K_{fq}^{hbmb} & K_{fr}^{hbms} & K_{fs}^{hbmt} \\ & K_{gq}^{1b1b} & K_{gr}^{1b1s} & K_{gs}^{1b1t} & 0 & 0 & 0 & 0 \\ & & K_{hr}^{1s1s} & K_{hs}^{1s1t} & \vdots & \vdots & \vdots & \vdots \\ & & & K_{is}^{1t1t} & 0 & \vdots & \vdots & \vdots \\ & & & & \ddots & 0 & 0 & 0 \\ & & & & & K_{gq}^{mbmb} & K_{gr}^{mbms} & K_{gs}^{mbmt} \\ & \text{sym} & & & & & K_{hr}^{msms} & K_{hs}^{msmt} \\ & & & & & & & K_{is}^{mtmt} \end{bmatrix} \tag{17}$$

$$\{q\} = \left\{ A_f^{hb} \quad B_g^{1b} \quad C_h^{1s} \quad D_i^{1t} \quad \cdots \quad B_g^{mb} \quad C_h^{ms} \quad D_i^{mt} \right\}^{\mathrm{T}} \tag{18}$$

$$\{F\} = \left\{ F_f^{hb} \quad 0 \quad 0 \quad 0 \quad \cdots \quad 0 \quad 0 \quad 0 \right\}^{\mathrm{T}} \tag{19}$$

The components of the damping matrix are $[C] = \alpha^m Re[M] + \beta^m Re[K]$, whereas the damping of the host tubular beam is $C_{fp}^{hbhb} = \alpha^h M_{fp}^{hbhb} + \beta^h K_{fp}^{hbhb}$. Thus, for the inclusions both viscous and structural damping mechanisms are accounted for [31]. The detailed components of the mass matrix $[M]$, stiffness matrix $[K]$, and force vector $\{F\}$ are listed in Appendix A. Solu-

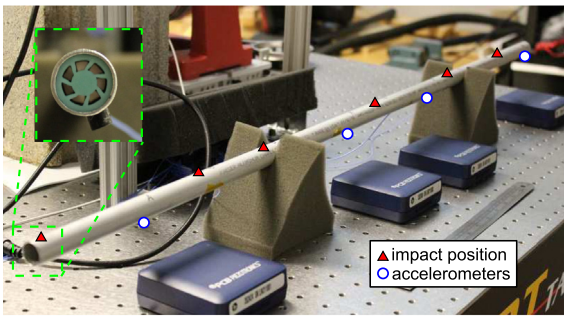

Fig. 2. Photograph of experimental setup.

tion to the components of unknown constants $\{q\}$ is obtained by Gauss elimination applied to Eq. (15). Then, substituting the unknown constants into Eq. (11), the lateral translation of the host, lateral translations, metamaterial shear angles, and metamaterial torsional angles of the inclusions are subsequently obtained.

4. Experimental setup

The experimental system is composed of a 0.91 m long hollow, circular cross-section aluminum tubular beam with embedded metamaterial inclusions, shown in Fig. 2. The inner radius R^h and outer radius R_o^h of the hollow, host beam are 8.28 mm and 9.53 mm, respectively. To constrain the metamaterial inclusion in the hollow beam, the outer radius of the inclusion (8.61 mm) is set to be 1.04 times the inner radius of the host tube. Two inclusions are fabricated for any given set of inclusion design parameters, so that one inclusion is placed at a given end of the host tube structure. The thickness of the annular metamaterial layer is 1.5 mm, i.e. $R^h - R^p$. This thickness dimension is selected to prevent warping of the annular metamaterial layer that is observed for inclusion specimens fabricated with much thinner annular layer thicknesses such as for annular layers only 0.5 mm thick. The inclusions adopted in this research have seven radially arrayed beams, i.e. $N = 7$, in the porous metamaterial layer. Based on the model composition presented in Section 3, inclusions with a different number of radially arrayed beams may also be studied. The metamaterial inclusions are made from silicone rubber (Smooth On Mold Star 15S) cast in 3D printed molds. A photo of the host beam with inclusions is shown in Fig. 2. The values of the normalized length of inclusions, the ratio of bulk to host radii, and the open angle ratio investigated in this report are selected according to fabrication capabilities and experiment feasibility. For example, the minimum thickness of the radially arrayed beams able to be fabricated by the casting method here is 0.3 mm. As a result, the minimum normalized radius of the core bulk metamaterial inclusion R^b/R^h is 0.12 when the open angle ratio α/β is 0.61. Furthermore, to avoid difficulty of repeatedly placing the inclusions into the circular hollow beam, the normalized radius of the bulk metamaterial inclusion R^b/R^h is set to be 0.22 when the normalized length of inclusion L^m/R^h is 6.04. This means that the longest inclusion considered is approximately 50 mm in comparison to the host beam length of 910 mm.

To simulate the free-free boundary condition, the host tubular beam is placed on two triangular foam supports that are randomly positioned to avoid suppressing particular modes of vibration. The foam stiffness when subjected to transverse compression is much less than the stiffnesses present in the system, and the contact areas between the foam and the host beam are small. As a result, the influences of the foam supports on the measured system responses are justifiably negligible [30].

The modal hammer experiments are conducted on the circular tube with or without metamaterial inclusions. The hammer (PCB 086C01) impacts at six locations, and accelerometers (PCB 352A24) read out acceleration data at four locations. The six impact locations and the four measurement locations are respectively represented by the filled triangle marks and unfilled circular marks in Fig. 2. Each experiment involves a total of 180 hits to generate the transfer function (TF) between output global acceleration and input force.

5. Experimental and analytical results and discussions

To validate the analytical model and investigate the influences of geometric parameters for vibration attenuation, a wide variety of metamaterial specimens are considered. By evaluating the respective influences of unique parameter changes on inclusion geometry, the following sub-sections reveal new knowledge on the exact interaction mechanisms between the constrained metamaterial inclusions and the host beam structure.

5.1. Analytical model solution details and assessment strategies

Based on the approach devised in Section 3, twenty trial functions are used in the Ritz expansion of the lateral displacement of the free-free host beam. For the free-free core bulk metamaterial inclusion, the lateral displacement, shear angle, and

torsional angle are expanded in the Ritz method assumed solutions using ten, eight, and eight trial functions, respectively. These numbers of trial functions are selected based on a convergence study that identified no significant change in analytical model predictions for greater number of trial functions in the frequency range of interest: 100–10,000 Hz. In the analytical model, to characterize the global vibration response of the host structure and inclusions the applied, lateral point forces to the beam are given at 201 randomly selected positions. The final force vector is the sum of all force vectors of the 201 random positions. This approach is found, through model studies, to yield a global vibration response of the system. Although the experiment is unable to yield as ideal global vibration response, the comparisons between analysis and experiment that follow in subsequent sub-sections suggests that the experiment mostly approaches the trends of a global response.

In this study, the validations are taken by comparison of the TF reduction and frequency reduction between experiment and analysis. The analytical TF between acceleration at the beam locations and the impact forces is obtained. The global TFs presented in narrowband studies are determined by the square root of the sum of squares of the TFs computed for each combination of acceleration evaluation and impact force location. The TF reductions are determined from the narrowband TFs in decibels of the host beam without inclusions subtracted from the TFs in decibels evaluated when the host beam has inclusions. To investigate the TF reductions for each mode, the frequency ranges for the six lowest order modes, over which the cumulative TF reductions are computed, are 85–180 Hz, 250–500 Hz, 500–890 Hz, 890–1450 Hz, 1450–2100 Hz, and 2100–2850 Hz. These ranges sufficiently encompass the six lowest order modes. Similarly, the resonant frequency reductions are found by tracking the peak amplitude of the narrowband TF in these frequency ranges as it shifts for the case of the host beam with inclusions compared to the case of the host beam without inclusions. Table 2 provides all of the relevant material

Table 2
Material properties of host structure and metamaterial inclusions.

	Young's modulus [Pa]	Poisson's ratio	density [kg/m^3]	structural loss factor	mass-proportional damping coefficient	stiffness-proportional damping coefficient
Beam	68.9×10^9	0.33	2700	0.0015	1×10^{-9}	1×10^{-9}
Inclusions	752×10^3	0.49	1145	0.02	5×10^{-5}	9×10^{-5}

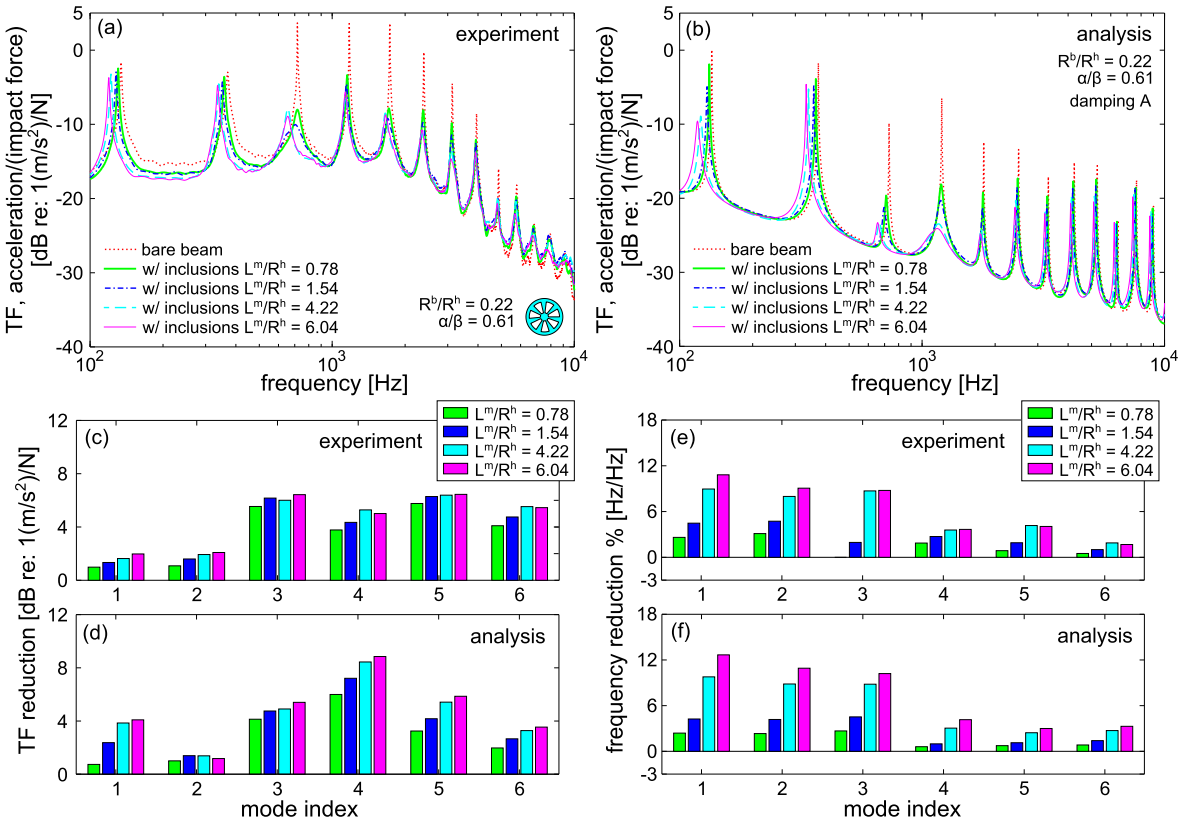

Fig. 3. (a) Experimental TF frequency responses, (b) analytical TF frequency responses, (c) experimental TF reductions, (d) analytical TF reductions, (e) experimental frequency reductions, and (f) analytical frequency reductions for four lengths of inclusions, L^m/R^h = 0.78, 1.54, 4.22, and 6.04. The radius ratio R^b/R^h is 0.22 while the open angle ratio α/β is 0.61.

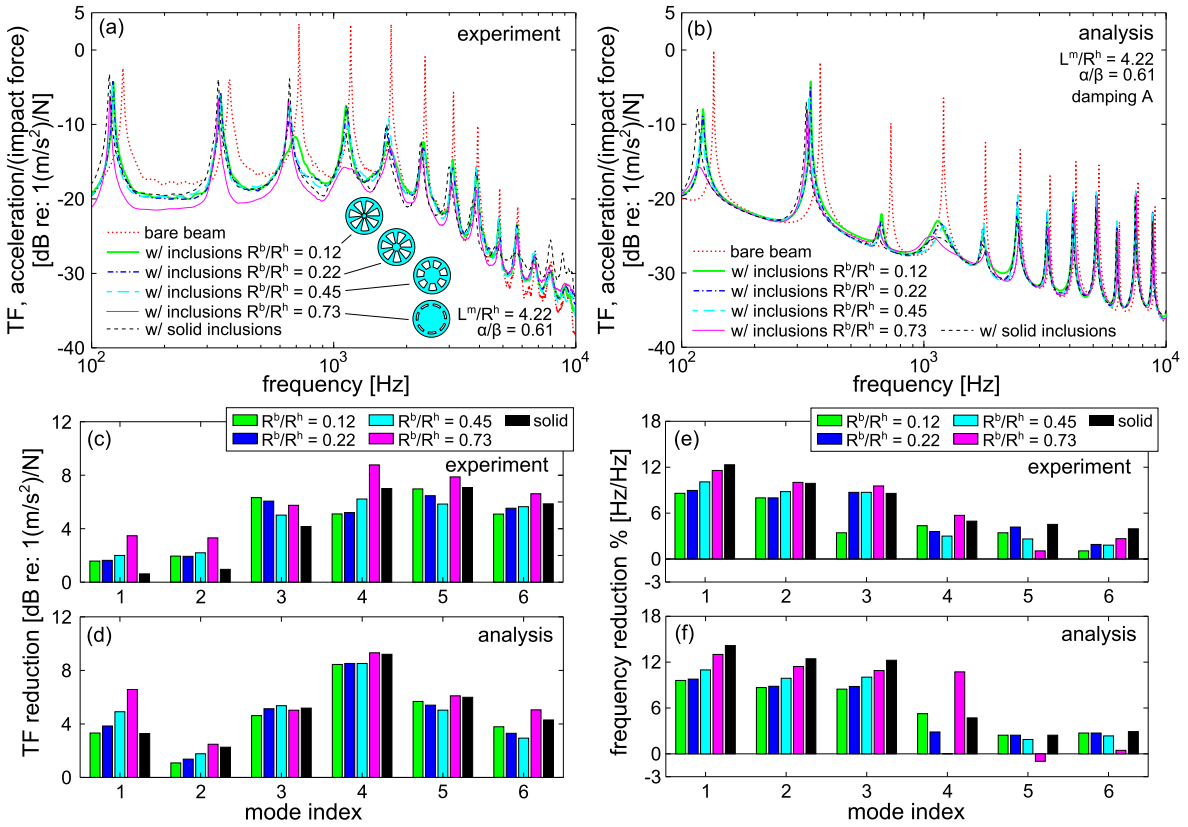

Fig. 4. (a) Experimental TF frequency responses, (b) analytical TF frequency responses, (c) experimental TF reduction, (d) analytical TF reduction, (e) experimental frequency reduction, and (f) analytical frequency reduction for four radii of core bulk metamaterial inclusions, R^b/R^h = 0.12, 0.22, 0.45, and 0.73, and for the solid inclusions. For the metamaterial inclusions, the length ratio L^m/R^h is 4.22 while the open angle ratio α/β is 0.61.

properties used in all analytical computations. The parameters are identified empirically from the experimental system. The remaining parameters used in the model to characterize unique inclusion designs are described in the respective subsections that follow.

5.2. Influences on length of metamaterial

The experimental and analytical frequency responses of the TFs are shown in Fig. 3 for four values of normalized lengths of inclusions, L^m/R^h = 0.77, 1.54, 4.22, and 6.04. For the metamaterials considered in Fig. 3, the ratio of bulk to host radii R^b/R^h is 0.22 while the open angle ratio α/β is 0.61.

In the results of Fig. 3 as well as for Figs. 4 and 5, there are a few minor discrepancies between the experiments and analytical predictions worth noting. For the six lowest order modes, the deviations between the experimental and analytical resonant frequencies of the bare beam are less than 5%. These discrepancies may be due to small imperfection in the knowledge of the host beam material properties. Also, the experimental TF of the bare beam does not reveal as great of amplitude at low and high frequencies as that in the model. This is caused by the modal impact hammer experimental technique that is challenged to induce wide-band frequency energy, which is due to the selection of an impact hammer tip that is necessarily best suited to inject energy within a finite range of frequencies. Despite these discrepancies, the observed influences in analysis and experiments of inserting the inclusions are found through Figs. 3–5 to be in relatively good agreement as discussed in this and the following sub-sections of Section 5. As such, the minor discrepancies between experiment and analysis described in this paragraph are concluded to be of negligible significance towards formulating conclusions regarding the interaction mechanisms observed between the inclusions and host.

While the narrowband experimental data, Fig. 3(a), and analytical predictions, Fig. 3(b), are in good overall agreement, the more synthesized results of Fig. 3(c)–(f) are of primary interest towards understanding the influences of change in the inclusion length. Specifically, Fig. 3(c) and (d) respectively present the experimental and analytical TF reductions of the lowest six modes for different length of inclusions. In general, the TF reduction increases for increase in the length of the inclusions. This result is intuitive on the basis of added mass increase with increase in inclusion length, so that the added mass or ballast helps to suppress the host beam vibration.

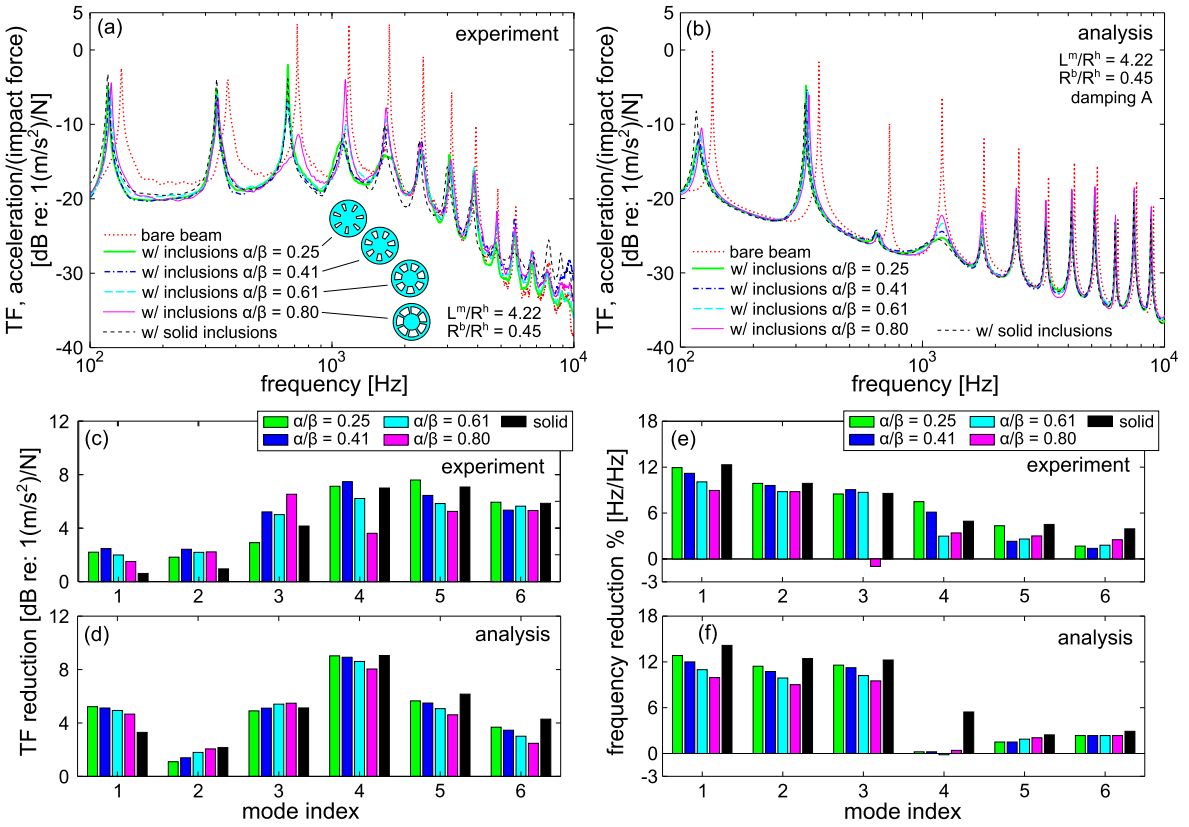

Fig. 5. (a) Experimental TF frequency responses, (b) analytical TF frequency responses, (c) experimental TF reduction, (d) analytical TF reduction, (e) experimental frequency reduction, and (f) analytical frequency reduction of the host beam with inclusions with four different open angle ratios of the radially arrayed beams, $\alpha/\beta = 0.25$, 0.41, 0.61, and 0.80, and for the solid inclusions. The length ratio L^m/R^h is 4.22 while the radius ratio R^b/R^h is 0.45.

Fig. 3(e) and (f) present the experimental and analytical frequency reductions of the lowest six modes for different length of inclusions, respectively. The frequency shift for each mode increases for increase in the length of the inclusions. The three lowest order modes have greater frequency reduction than the fourth, fifth, and sixth modes in both experimental and analytical results. The unique modal dependence of the frequency shifts will be more fully assessed in Section 5.7. Overall, the experiment and analysis exemplify strong agreement on the roles of changing inclusion length on the system dynamic response.

5.3. Influences on radius of core bulk metamaterial

Fig. 4(a) and (b) respectively present the experimental and analytical TF frequency responses for four values of the normalized radii of core bulk metamaterial inclusions, $R^b/R^h = 0.12$, 0.22, 0.45, and 0.73, and for the solid inclusions. In the experiments, the solid inclusions are solid cylinders of the bulk silicone rubber material that are inserted and held in the hollow tube using a small compression fit. In the analysis, the solid inclusions are realized by the special case of $R^b/R^h = 0.01$ and $\alpha/\beta = 0.01$. For the metamaterials considered in Fig. 4, the normalized length L^m/R^h is 4.22 and the open angle ratio α/β is 0.61. The experimental and analytical TF reductions of the lowest six order modes for different radius of core bulk metamaterials and solid inclusions are shown in Fig. 4(c) and (d), respectively. When the core radius of the inclusion increases, the inclusion core is more massive. For the same increase in core radius, when the open angle ratio α/β is constant, the radially arrayed beams in the porous metamaterial layer are shorter so as to increase the bending and shear stiffnesses induced for radially arrayed beam deformation. For modes 1, 2, 4 and 6, the TF reductions increase for greater radius of the inclusion cores, a trend seen in both experiments and analysis of Fig. 4(c) and (d). In contrast, there is less influence on the TF reduction for the third mode.

Modifications to the core radius may tailor all of the interaction mechanisms engaged by translational, shear, and torsional deformations between the core and host structure. The results suggest that the inclusion considered in Fig. 4 with the largest core size $R^b/R^h = 0.73$ has a more substantial capability to reduce the TF amplitudes of the six lowest order modes. Excepting for the result for the third mode, the inclusion with $R^b/R^h = 0.73$ delivers greater vibration attenuation of the six

lowest order modes than the solid inclusions. Indeed, there is a particularly wide frequency bandwidth of vibration attenuation from 891 to 1415 Hz, i.e. around the fourth resonant frequency, in both experimental and analytical TF frequency responses when $R^b/R^h = 0.73$ in Fig. 4(a) and (b). Considering the trends observed for change in the inclusion core radius, an analogy to CLD is possible. In other words, the core bulk metamaterial layer, thin porous metamaterial layer of radially arrayed beam, and the host beam structure may be analogous to the constrained layer, viscoelastic layer, and the host structure sought to be damped, respectively. As a result, it may be concluded that the inclusions with $R^b/R^h = 0.73$ have greater reductions for each mode due to CLD-like effects. This is because that, like traditional CLD concepts [32], the greater core diameter and shorter radially arrayed beams exert higher shear and bending stresses in the radially arrayed beams (porous metamaterial layer) for broadband energy dissipation.

Fig. 4(e) and (f) present the corresponding experimental and analytical frequency reductions for the six lowest order modes. For the lowest three modes, both experiment and analysis agree that the frequency reduction increases when the core radius increases. This trend is likely due to the corresponding mass increase provided by the inclusions with greater core radii. Except for the fourth modes, the solid inclusions have greater frequency reductions for each mode due to mass increase in both experimental and analytical results. For the fourth mode, the inclusion with $R^b/R^h = 0.73$ has the greatest frequency reduction. There is respectively little change in the resonant frequencies of the fifth and sixth modes, a trend seen experimentally and analytically. All together, these unique interaction mechanisms that tailor the TF amplitudes and resonant frequencies are characterized by the analysis and likewise observed in the experimental data trends.

5.4. Influences on open angle ratio α/β

Fig. 5(a) and (b) respectively present the experimental and analytical TF frequency responses for four values of the open angle ratio of the radially arrayed beams, $\alpha/\beta = 0.25$, 0.41, 0.61, and 0.80, and for the solid inclusions. For the metamaterials considered in Fig. 5, the normalized length L^m/R^h is 4.22 and the normalized radius of the core bulk metamaterial inclusion R^b/R^h is 0.45. The experimental and analytical TF reductions for four open angle ratios and the solid inclusions of the lowest six modes are shown in Fig. 5(c) and (d). For an increase in the open angle ratio α/β, the radially arrayed beams in the porous metamaterial layer become less massive and more slender. It is thus assumed that such influence of increasing open angle ratio provides an increasingly softer and lighter interface between the metamaterial inclusion core and the host structure. As seen in Fig. 5(c) and (d), when the open angle ratio increases, the TF reduction slightly decreases except for the second and third modes. Correspondingly, when the open angle ratio increases, the mass of the inclusion decreases while the dynamic stiffness of the porous metamaterial layer is also decreased since the radially arrayed beams become more slender.

Fig. 5(e) and (f) shows the experimental and analytical frequency reductions of the lowest six modes. Except for the fourth mode in the experimental result, the solid inclusions have the greatest frequency reduction due to mass increase. Overall, for the lowest three modes, the trend is that the frequency reduction slightly decreases when the open angle ratio increases, potentially explained by the decreasing metamaterial inclusion mass for greater open angle ratios.

5.5. Existence of TMD vibration attenuation phenomena

In Figs. 3(a), 4(a), and 5(a), large vibration attenuation is observed at frequencies around the third or fourth mode of the host structure, i.e. in the frequency range from around 700 to 1500 Hz. This is borne out experimentally and analytically and seen for many of the metamaterial inclusions examined in this research. For instance, one may observe large vibration suppression around the third and fourth modes when the inclusions are designed using normalized radii $R^b/R^h = 0.45$ and R^b/R^h

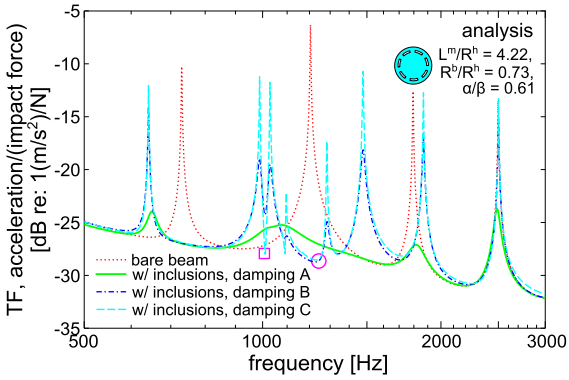

Fig. 6. Analytical TF frequency responses of host beam with the inclusions with three set of damping values, including damping A: $\eta^m = 0.02$, $\alpha^m = 5 \times 10^{-5}$, $\beta^m = 9 \times 10^{-5}$; damping B: $\eta^m = 0.02$, $\alpha^m = 1 \times 10^{-7}$, $\beta^m = 2 \times 10^{-7}$; and damping C: $\eta^m = 0.002$, $\alpha^m = 1 \times 10^{-9}$, $\beta^m = 2 \times 10^{-9}$. The length L^m/R^h is 4.22, the radius ratio R^b/R^h is 0.73, and the open angle ratio α/β is 0.61.

= 0.73 as shown in Fig. 4(a), or when the inclusions are created with open angle ratio α/β = 0.25, 0.41, and 0.61, as shown in Fig. 5(a).

To examine the origins of such unique mode dependent vibration attenuation, the analytical model is further leveraged. Fig. 6 presents the analytical TF frequency responses for cases of inclusions having three damping models realized by distinct contributions from the structural loss factor η^m, mass-proportional damping coefficient α^m, and stiffness-proportional damping coefficient β^m. The parameter combinations examined are damping A: $\eta^m = 0.02$, $\alpha^m = 5 \times 10^{-5}$, $\beta^m = 9 \times 10^{-5}$; damping B: $\eta^m = 0.02$, $\alpha^m = 1 \times 10^{-7}$, $\beta^m = 2 \times 10^{-7}$; and damping C: $\eta^m = 0.002$, $\alpha^m = 1 \times 10^{-9}$, $\beta^m = 2 \times 10^{-9}$. For the metamaterials considered in Fig. 6, the normalized length L^m/R^h is 4.22, the normalized radius R^b/R^h is 0.73, and the open angle ratio α/β is 0.61. The resonant frequency of the fourth mode is observed at 1078 Hz when for the case of damping A with $\eta^m = 0.02$, $\alpha^m = 5 \times 10^{-5}$, $\beta^m = 9 \times 10^{-5}$ shown by the green solid curve in Fig. 6. When the damping in the inclusions slightly decreases to damping B with $\eta^m = 0.02$, $\alpha^m = 1 \times 10^{-7}$, $\beta^m = 2 \times 10^{-7}$ shown by the blue dash-dot curve in Fig. 6, a narrowband attenuation of the TF is observed at 1010 Hz, around the third and fourth modes. With a further decrease in damping in the inclusions to damping C with $\eta^m = 0.002$, $\alpha^m = 1 \times 10^{-9}$, $\beta^m = 2 \times 10^{-9}$ shown by the cyan dashed curve in Fig. 6, a local minima of TF, termed a "notch", at 1010 Hz becomes more apparent and results in two large resonances at adjacent frequencies, in a manner similar to TMD influences upon a host structure. In addition, a second and notable reduction of the TF becomes more prominent around 1223 Hz, i.e. around the fourth mode. Based on the understanding that such notches are eliminated by an increase in damping, it is concluded that these narrowband attenuation zones are evidence of TMD-like behaviors provided by the metamaterial inclusions. Pai et al. [1,3] also found that increase in damping decreased such more dramatic, narrowband frequency response function attenuation.

To explore the mechanisms by which the metamaterial inclusions exert forces on the host beam to attenuate the vibration, Fig. 7 shows the analytical predictions of displacements along the host beam and metamaterial lengths. Fig. 7(a) presents the translational displacements for the host structure with and without metamaterial inclusions at 1223 Hz where the parameters are taken from the study of Fig. 6: L^m/R^h = 4.22, R^b/R^h = 0.73, α/β = 0.61, and the damping C model for the inclusions with $\eta^m = 0.002$, $\alpha^m = 1 \times 10^{-9}$, and $\beta^m = 2 \times 10^{-9}$. The frequency from Fig. 6 for which the spatial plots in Fig. 7 are generated is 1223 Hz, which is highlighted by the circle marker in Fig. 6. Fig. 7(a) shows that the bare beam exhibits large lateral vibration that is greatly suppressed by the inclusions. To investigate the TMD-like behavior at 1223 Hz, the bending, shear, and torsional displacements of the inclusions are computed. Here, bending and torsional displacements are the displacement in the z axis induced by bending deformation and torsion of the inclusion, respectively. Shear displacement is defined by the displacement in the x axis in the xz plane induced by the shear angle of the inclusion. For the fourth mode TF notch, the bending, shear, and torsional displacements of the inclusions placed at the left and right ends of the host struc-

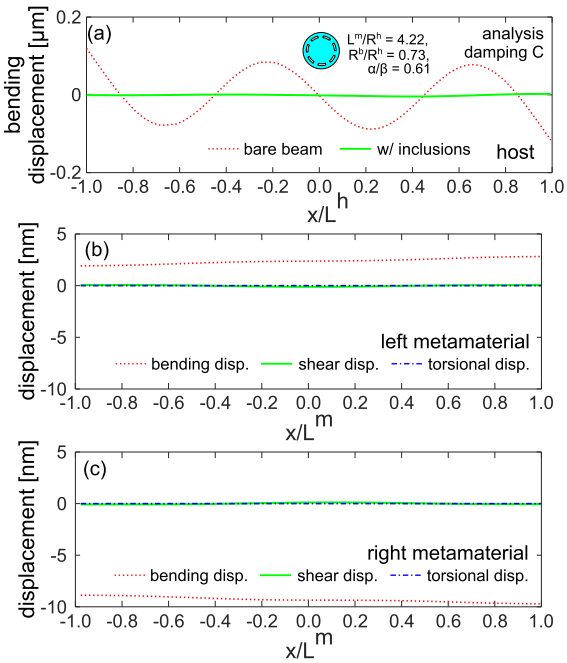

Fig. 7. (a) Analytical spatial translational displacements of host structure with and without metamaterial inclusions with L^m/R^h = 4.22, R^b/R^h = 0.73, α/β = 0.61, $\eta^m = 0.002$, $\alpha^m = 1 \times 10^{-9}$, and $\beta^m = 2 \times 10^{-9}$ at 1223 Hz. (b) Displacement responses of left metamaterial. (c) Displacement responses of right metamaterial.

ture are shown in Fig. 7(b) and (c), respectively. The inclusions have greater translational (i.e. bending) deformation than shear and torsional deformations. In other words, the inclusions deliver an anti-phase lateral force to attenuate the motion of the host structure. It can be concluded that the TMD behavior at 1223 Hz is induced by bending deformations of the inclusions, encouraging a term "bending TMD behavior".

The inclusion deformations are shown at 1010 Hz, i.e. around the third and fourth modes of the host beam, in Fig. 8 for the case of inclusion damping model C using $\eta^m = 0.002$, $\alpha^m = 1 \times 10^{-9}$, and $\beta^m = 2 \times 10^{-9}$. This frequency is highlighted in Fig. 6 by the square marker. In Fig. 8, it is seen that the inclusions undergo greater shear deformations in comparison to the translational and torsional deformations. In other words, for the TMD behavior around the third and fourth modes, the cross-sections of the inclusions rotate in the y-axis, in a way to rock back-and-forth to attenuate the beam vibration. It can be concluded that the TMD behavior at 1010 Hz is induced by shear deformations of the inclusions, encouraging the term a "shear TMD behavior".

The bending and shear deformations are analogous to two degrees-of-freedom. As a result, the metamaterial inclusions studied in this research may be conceptualized as two-degree-of-freedom TMDs according to the distinct ways by which they interact with the host structure. In other words, one metamaterial inclusion achieves a combination of influences comparable to a two-degree-of-freedom TMD. Consequently, this study reveals that multiple interactions mechanisms of the metamaterial inclusions may enhance the versatility of vibration attenuation using fewer attached treatments.

5.6. Adaptation of shear TMD vibration attenuation phenomena

The results of Section 5.5 indicate that the metamaterials exhibit multiple TMD-like mechanisms by which to control the host beam vibration. To uncover strategies to tailor the working frequency range for the shear TMD phenomena, Fig. 9(a) presents the analytical TF frequency response of the host beam with the metamaterial inclusions for three values of the open angle ratio of the radially arrayed beams, α/β = 0.25, 0.50, and 0.75. For the metamaterials considered in Fig. 9(a), the normalized length L^m/R^h is 4.22, the normalized radius of the core bulk metamaterial inclusion R^b/R^h is 0.50, and the inclusion damping coefficients are $\eta^m = 0.02$, $\alpha^m = 1 \times 10^{-7}$, and $\beta^m = 2 \times 10^{-7}$. Additional parameters used in the analysis for the results of Fig. 9 are reported in Table 2.

In Fig. 9(a), one observes a first notch, around the third and fourth modes, at 912 Hz for α/β = 0.25. As the open angle ratio is varied to α/β = 0.50 the notch shifts downwards to 907 Hz and still further downwards to 876 Hz for α/β = 0.75. Assessing the influences on the inclusion geometry with the parameter chance, for increase in the open angle ratio α/β the total inclusion mass reduces while the overall dynamic stiffness of the porous metamaterial layer decreases. Stiffness reduction (without mass change) reduces the frequency of a TMD behavior, whereas mass reduction (without stiffness change) increases the frequency of a TMD behavior. Based on the trends of decreasing notch frequency by increasing the open angle ratio α/β, it is apparent that the most influential aspect of tailoring the open angle ratio of the inclusions is to change the dynamic stiffness of the overall porous layer and thus result in a decrease of the notch frequency.

Fig. 9(b) presents the analytical TF frequency responses of the host beam with the metamaterial inclusions when the normalized radius of the core bulk metamaterial inclusion is either R^b/R^h = 0.25, 0.50, or 0.75. For the metamaterials considered in Fig. 9(b), the normalized length L^m/R^h is 4.22, the open angle ratio of the radially arrayed beams α/β is 0.25, and the inclusion damping coefficients are $\eta^m = 0.02$, $\alpha^m = 1 \times 10^{-7}$, and $\beta^m = 2 \times 10^{-7}$. In Fig. 9(b), one observes how change of the normalized radius of the central core layer of the metamaterial inclusion tailors the significance of the TMD behaviors. For

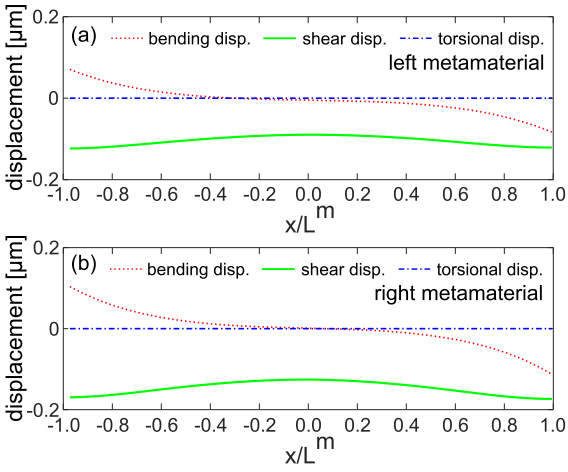

Fig. 8. (a) Analytical displacement responses of left metamaterial. (b) Displacement responses of right metamaterial. Results at frequency 1010 Hz. Parameters used are L^m/R^h = 4.22, R^b/R^h = 0.73, α/β = 0.61, $\eta^m = 0.002$, $\alpha^m = 1 \times 10^{-9}$, and $\beta^m = 2 \times 10^{-9}$.

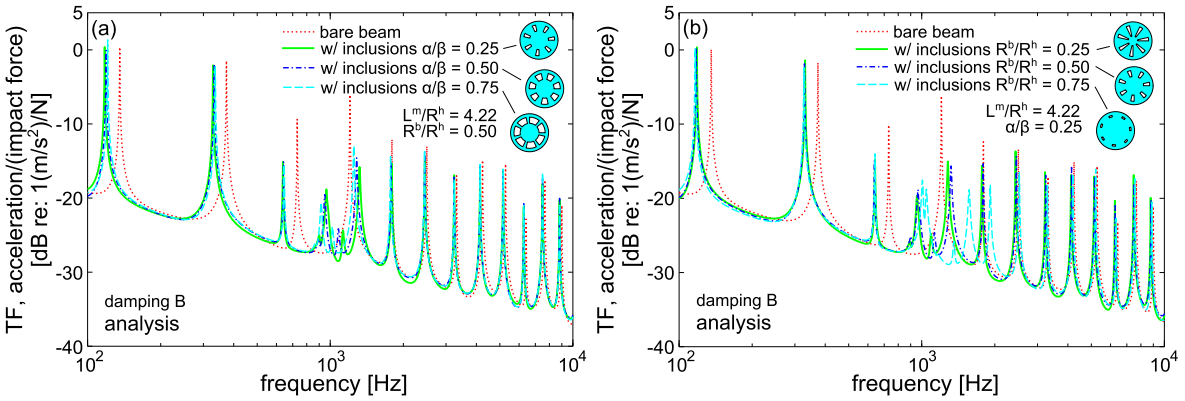

Fig. 9. (a) Analytical TF frequency responses of host beam with the inclusions with three values for open angle ratio, α/β= 0.25, 0.50, and 0.75. The length L^m/R^h is 4.22, and the radius ratio R^b/R^h is 0.50. (b) Analytical TF frequency responses of host beam with the inclusions with three values for radius ratio R^b/R^h is 0.25, 0.50, and 0.75. The length L^m/R^h is 4.22, and the open angle ratio α/β is 0.25.

instance, a first notch occurs around the third and fourth modes at 902 Hz for R^b/R^h = 0.25, then shifts upwards to 912 Hz for R^b/R^h = 0.50, and shifts further to higher frequencies around 1027 Hz for R^b/R^h = 0.75. The increase in the normalized radius R^b/R^h of the core layer of the metamaterial inclusion results in an increase in the dynamic mass yet also reduces the length of the radially arrayed beams without changing the beam thickness. The latter influence thus increases the overall dynamic stiffness of the porous metamaterial layer. The results of Fig. 9(b) suggest that the increase in the normalized radius R^b/R^h leads to an increase in the notch frequency. Consequently, the change of the normalized radius R^b/R^h, all other metamaterial inclusion parameters remaining the same, is more influential to change the overall stiffness of the inclusions than to change the dynamic mass.

Generally, shear deformation is more influential for thick beams than for slender beams. When the open angle ratio α/β reduces, the radially arrayed beams become thicker (i.e. reduced slenderness) so as to increase the amplitude of shear displacement. When the normalized radius R^b/R^h increases, the radially arrayed beams also become less slender. These parameter changes using α/β and R^b/R^h help to govern the activation of the shear TMD effect.

5.7. Adaptation of bending TMD vibration attenuation phenomena

As shown through the results of Fig. 7, at frequencies around fourth mode of the host structure the primary deformation of the inclusions is lateral translation associated with relative displacement between the bulk metamaterial layer and host structure. Small changes in such bending TMD effect are observed through the shifting of the notch in Fig. 9(a) and (b) according to change in the parameters of open angle ratio α/β and the radius ratio R^b/R^h. Yet, change in other design parameters may be more influential to tailor the dynamics associated with the bending TMD behavior.

To investigate the parameter that may greatly influence the existence of such bending TMD effects, Fig. 10 presents the analytical TF frequency responses of the host beam with the metamaterial inclusions for three values of Young's modulus,

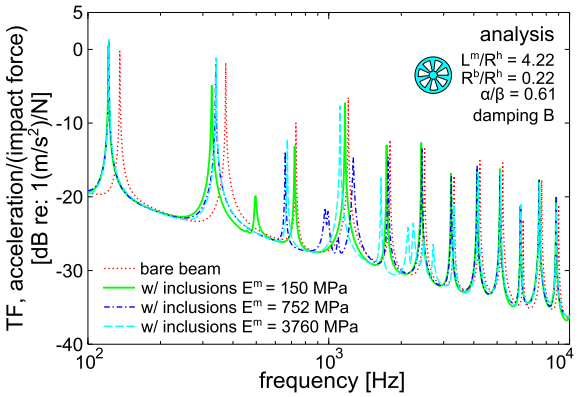

Fig. 10. Analytical TF frequency responses of host beam with the inclusions with three values for Young's modulus, E^m= 150 MPa, 752 MPa, and 3760 MPa. The length L^m/R^h is 4.22, the radius ratio R^b/R^h is 0.22, and the open angle ratio α/β is 0.61.

E^m = 150 MPa, 752 MPa, and 3760 MPa. For the metamaterials considered in Fig. 10, the normalized length L^m/R^h is 4.22, the normalized radius of the core bulk metamaterial inclusion R^b/R^h is 0.22, the open angle ratio of the radially arrayed beams α/β is 0.61, and the inclusion damping coefficients are from the damping model B using $\eta^m = 0.02$, $\alpha^m = 1 \times 10^{-7}$, and $\beta^m = 2 \times 10^{-7}$.

As seen in Fig. 10, for an increase of the Young's modulus of the inclusions, the resonant frequency at which the bending TMD behavior occurs increases. In Figs. 3(e), 4(e), and 5(e), the frequency shifts for the fourth, fifth, and sixth modes are seen to be less than the frequency shifts induced for the three lowest order modes. For the metamaterials considered in Figs. 3–5, the bending TMD effects all occur at the frequencies around the third and the fourth modes since the Young's modulus values are the same for all of the results presented in Figs. 3–5. Consequently, it is apparent that the smaller frequency shifts of the higher modes are associated with frequencies greater than the bending TMD behavior. In Fig. 10, for the metamaterial inclusions with Young's modulus E^m = 150 MPa, the resonant frequency of the bending TMD is at the frequency around the second and third mode, in the frequency range around 400–600 Hz. For this selection of the Young's modulus, the modal frequency shifts are less from the third mode and above, than for the first and second modes. For the case of the metamaterial inclusions with Young's modulus E^m = 3760 MPa in Fig. 10, the resonant frequency of bending TMD is around the fifth and sixth modes, in the frequency range from around 1900 to 3000 Hz. Consequently, the reduced shifts of the modal resonant frequencies are apparent for modes greater than the sixth mode. These results reveal that the significance of the resonant frequency shifts is associated with the frequencies around which the bending TMD behaviors occur. At frequencies greater than this range, the resonant frequency shifts are significantly reduced.

6. Conclusions

This research establishes and experimentally validates an analytical modeling framework to elucidate the working mechanisms of broadband vibration attenuation realized by elastomeric metamaterial inclusions within host cylindrical structures. Leveraging the analysis reveals a wealth of non-intuitive insight on the specific ways by which the elastomeric inclusions couple with the host structure. For instance, change in open angle ratio of the inclusion cross-section geometry and change in the central core mass diameter are primarily stiffness-tuning mechanisms although one may anticipate that the more visually apparent mass changes may be more influential. While the open angle ratio and radius ratio parameters are seen to slightly influence frequency range and depth of the notch-like vibration attenuation features, only change of the radius ratio influences bending TMD effects at higher frequencies. In addition, the Young's modulus of the metamaterial inclusions is another means by which to dramatically shift the frequencies at which the bending TMD phenomena occur. Overall, this work uncovers the specific existence and adaptation mechanisms of two distinct TMD behaviors manifest by the single metamaterial inclusion design, paving the way for future designs of broadband vibration mitigation material systems.

Acknowledgments

This work is supported by The Ohio State University Simulation Innovation and Modeling Center via Honda R&D Americas, Inc.

Appendix A

A.1. Constants of area and area moment inertia

$$A^h = \pi\left[\left(R_o^h\right)^2 - \left(R^h\right)^2\right] \tag{A.1}$$

$$A_{31}^b = A_{51}^b = A_{52}^b = \pi\left(R^b\right)^2 \tag{A.2}$$

$$A_{57}^b = 2\pi\left(R^b\right)^2 \tag{A.3}$$

$$A_{30}^a = \frac{\pi}{6\left(R^h - R^b\right)^2}\left\{\begin{array}{c} 6\left(R^b\right)^2\left[\left(R^h\right)^2 - (R^p)^2\right] \\ -8R^b\left[\left(R^h\right)^3 - (R^p)^3\right] + 3\left[\left(R^h\right)^4 - (R^p)^4\right] \end{array}\right\} \tag{A.4}$$

$$A_{31}^{a} = \frac{\pi}{6\left(R^{h} - R^{b}\right)^{2}}\left(R^{h} - R^{p}\right)^{3}\left(R^{h} + 3R^{p}\right) \tag{A.5}$$

$$A_{34}^{a} = \frac{\pi\left(R^{h} - R^{p}\right)^{2}}{3\left(R^{h} - R^{b}\right)^{2}}\left[\left(R^{h}\right)^{2} + 2\left(R^{h}\right)(R^{p}) + 3(R^{p})^{2} - 2\left(R^{b}\right)\left(R^{h} + 2R^{p}\right)\right] \tag{A.6}$$

$$A_{50}^{a} = \frac{3\pi\left[\left(R^{h}\right)^{4} - (R^{p})^{4}\right]}{16\left(R^{h} - R^{b}\right)^{2}} \tag{A.7}$$

$$A_{51}^{a} = \frac{\pi\left(R^{h} - R^{p}\right)^{3}\left(R^{h} + 3R^{p}\right)}{6\left(R^{h} - R^{b}\right)^{2}} \tag{A.8}$$

$$A_{52}^{a} = \frac{\pi}{16\left(R^{h} - R^{b}\right)^{2}}\left[3\left(R^{h}\right)^{4} - 16\left(R^{h}\right)^{2}(R^{p})^{2} + 32R^{h}(R^{p})^{3} - 19(R^{p})^{4}\right] \tag{A.9}$$

$$A_{54}^{a} = \frac{\pi}{6\left(R^{h} - R^{b}\right)^{2}}\left[\left(R^{h}\right)^{4} - 4R^{h}(R^{p})^{3} + 3(R^{p})^{4}\right] \tag{A.10}$$

$$A_{55}^{a} = \frac{\pi}{24\left(R^{h} - R^{b}\right)^{2}}\left[5\left(R^{h}\right)^{4} + 16R^{h}(R^{p})^{3} - 21(R^{p})^{4}\right] \tag{A.11}$$

$$A_{57}^{a} = -\frac{\pi\left(R^{h} - R^{p}\right)^{2}}{6\left(R^{h} - R^{b}\right)^{2}}\left[\left(R^{h}\right)^{2} + 2R^{h}R^{p} - 9(R^{p})^{2}\right] \tag{A.12}$$

$$A_{60}^{a} = A_{62}^{a} = \frac{\pi\left[\left(R^{h}\right)^{4} - (R^{p})^{4}\right]}{16\left(R^{h} - R^{b}\right)^{2}} \tag{A.13}$$

$$A_{65}^{a} = \frac{\pi\left[\left(R^{h}\right)^{4} - (R^{p})^{4}\right]}{8\left(R^{h} - R^{b}\right)^{2}} = 2A_{60}^{a} \tag{A.14}$$

$$A_{23}^{p} = A_{33}^{p} = \frac{\left(R^{b}\right)^{4} - (R^{p})^{4}}{128\left(R^{h} - R^{b}\right)^{2}}\Theta_{21} \tag{A.15}$$

$$A_{30}^{p} = \frac{\Theta_{0}}{12\left(R^{h} - R^{b}\right)^{2}}\left(R^{b} - R^{p}\right)^{3}\left(R^{b} + 3R^{p}\right) \tag{A.16}$$

$$A_{31}^{p} = \frac{\Theta_{0}}{12\left(R^{h} - R^{b}\right)^{2}}\begin{bmatrix} 3\left(R^{b}\right)^{4} - 8\left(R^{b}\right)^{3}\left(R^{h}\right) + 6\left(R^{b}\right)^{2}\left(R^{h}\right)^{2} \\ -3(R^{p})^{4} + 8(R^{p})^{3}\left(R^{h}\right) - 6(R^{p})^{2}\left(R^{h}\right)^{2} \end{bmatrix} \tag{A.17}$$

$$A_{34}^{p} = \frac{\Theta_{0}\left(R^{b} - R^{p}\right)^{2}}{6\left(R^{h} - R^{b}\right)^{2}}\left[\left(R^{b}\right)^{2} - 2\left(R^{b}\right)\left(R^{h}\right) + 2\left(R^{b}\right)(R^{p}) - 4\left(R^{h}\right)(R^{p}) + 3(R^{p})^{2}\right] \tag{A.18}$$

$$A_{43}^{p}=\frac{\left(R^{b}\right)^{4}-\left(R^{p}\right)^{4}}{32\left(R^{b}-R^{h}\right)^{2}}\Theta_{22} \tag{A.19}$$

$$A_{50}^{p}=\frac{\left(R^{b}\right)^{4}-\left(R^{p}\right)^{4}}{128\left(R^{h}-R^{b}\right)^{2}}\Theta_{8} \tag{A.20}$$

$$A_{51}^{p}=\frac{\Theta_{0}}{12\left(R^{h}-R^{b}\right)^{2}}\left\{\begin{array}{l}3\left(R^{b}\right)^{4}-8\left(R^{b}\right)^{3}\left(R^{h}\right)+6\left(R^{b}\right)^{2}\left(R^{h}\right)^{2}\\+\left(R^{p}\right)^{2}\left[-6\left(R^{h}\right)^{2}+8\left(R^{p}\right)\left(R^{h}\right)-3\left(R^{p}\right)^{2}\right]\end{array}\right\} \tag{A.21}$$

$$A_{52}^{p}=\frac{1}{384\left(R^{h}-R^{b}\right)^{2}}\left\{\begin{array}{l}12\left(R^{b}-R^{p}\right)\left[\begin{array}{c}19\left(R^{b}\right)^{3}+\left(R^{p}\right)^{2}\left(-32R^{h}+19R^{b}\right)\\+\left(R^{b}+R^{p}\right)\left[16\left(R^{h}\right)^{2}-32\left(R^{h}\right)\left(R^{b}\right)+19\left(R^{b}\right)^{2}\right]\end{array}\right]\Theta_{0}\\-8\left[9\left(R^{b}\right)^{4}-8\left(R^{b}\right)^{3}\left(R^{h}\right)+\left(8R^{h}-9R^{p}\right)\left(R^{p}\right)^{3}\right]\Theta_{62}\\+3\left[\left(R^{b}\right)^{4}-\left(R^{p}\right)^{4}\right]\Theta_{63}\end{array}\right\} \tag{A.22}$$

$$A_{54}^{p}=-\frac{\Theta_{11}}{12\left(R^{h}-R^{b}\right)^{2}}\left[3\left(R^{b}\right)^{4}-4\left(R^{b}\right)^{3}\left(R^{h}\right)+\left(4R^{h}-3R^{p}\right)\left(R^{p}\right)^{3}\right] \tag{A.23}$$

$$A_{55}^{p}=\frac{1}{192\left(R^{h}-R^{b}\right)^{2}}\left\{-\left(R^{b}\right)^{3}\left[64\left(R^{h}\right)\Theta_{11}+3\left(R^{b}\right)\Theta_{4}\right]+\left(R^{p}\right)^{3}\left[64\left(R^{h}\right)\Theta_{11}+3\left(R^{p}\right)\Theta_{4}\right]\right\} \tag{A.24}$$

$$A_{57}^{p}=\frac{1}{24\left(R^{h}-R^{b}\right)^{2}}\left\{\begin{array}{l}-2\left(R^{b}\right)^{2}\left[9\left(R^{b}\right)^{2}-20\left(R^{b}\right)\left(R^{h}\right)+12\left(R^{h}\right)^{2}\right]\Theta_{0}\\+2\left(R^{p}\right)^{2}\left[12\left(R^{h}\right)^{2}-20\left(R^{h}\right)\left(R^{p}\right)+9\left(R^{p}\right)^{2}\right]\Theta_{0}\\+\left(R^{b}\right)^{3}\left(3R^{b}-4R^{h}\right)\Theta_{62}\\-\left(R^{p}\right)^{3}\left(-4R^{h}+3R^{p}\right)\Theta_{62}\end{array}\right\} \tag{A.25}$$

$$A_{60}^{p}=A_{62}^{p}=\frac{\left(R^{b}\right)^{4}-\left(R^{p}\right)^{4}}{128\left(R^{h}-R^{b}\right)^{2}}\Theta_{21} \tag{A.26}$$

$$A_{65}^{p}=\frac{\left(R^{b}\right)^{4}-\left(R^{p}\right)^{4}}{64\left(R^{h}-R^{b}\right)^{2}}\Theta_{21}=2A_{60}^{p} \tag{A.27}$$

$$I^{h}=\frac{\pi}{4}\left[\left(R_{o}^{h}\right)^{4}-\left(R^{h}\right)^{4}\right] \tag{A.28}$$

$$I_{12}^{b}=I_{23}^{b}=I_{33}^{b}=\frac{\pi}{4}\left(R^{b}\right)^{4} \tag{A.29}$$

$$I_{10}^{a}=\frac{\pi}{\left(R^{h}-R^{b}\right)^{2}}\left\{\frac{\left(R^{b}\right)^{2}}{4}\left[\left(R^{h}\right)^{4}-\left(R^{p}\right)^{4}\right]-\frac{2R^{b}}{5}\left[\left(R^{h}\right)^{5}-\left(R^{p}\right)^{5}\right]+\frac{1}{6}\left[\left(R^{h}\right)^{6}-\left(R^{p}\right)^{6}\right]\right\} \tag{A.30}$$

$$I_{12}^{a}=\frac{\pi}{60\left(R^{h}-R^{b}\right)^{2}}\left[\left(R^{h}\right)^{6}-15\left(R^{h}\right)^{2}(R^{p})^{4}+24R^{h}(R^{p})^{5}-10(R^{p})^{6}\right] \tag{A.31}$$

$$I_{15}^{a}=\frac{\pi}{30\left(R^{h}-R^{b}\right)^{2}}\begin{bmatrix}\left(R^{h}\right)^{5}\left(-3R^{b}+2R^{h}\right)+15R^{b}R^{h}(R^{p})^{4}\\-12\left(R^{b}+R^{h}\right)(R^{p})^{5}+10(R^{p})^{6}\end{bmatrix} \tag{A.32}$$

$$I_{30}^{a}=I_{31}^{a}=\frac{\pi\left[\left(R^{h}\right)^{2}-(R^{p})^{2}\right]}{2\left(R^{h}-R^{b}\right)^{2}} \tag{A.33}$$

$$I_{34}^{a}=\frac{\pi\left[\left(R^{h}\right)^{2}-(R^{p})^{2}\right]}{\left(R^{h}-R^{b}\right)^{2}}=2I_{30}^{a} \tag{A.34}$$

$$I_{10}^{p}=\frac{\Theta_{11}}{120\left(R^{h}-R^{b}\right)^{2}}\left[\left(R^{b}\right)^{6}-15\left(R^{b}\right)^{2}(R^{p})^{4}+24\left(R^{b}\right)(R^{p})^{5}-10(R^{p})^{6}\right] \tag{A.35}$$

$$I_{12}^{p}=I_{23}^{p}=\frac{\Theta_{11}}{120\left(R^{h}-R^{b}\right)^{2}}\left\{\begin{array}{c}10\left(R^{b}\right)^{6}-24\left(R^{b}\right)^{5}\left(R^{h}\right)+15\left(R^{b}\right)^{4}\left(R^{h}\right)^{2}\\+(R^{p})^{4}\left[-15\left(R^{h}\right)^{2}+24\left(R^{h}\right)(R^{p})-10(R^{p})^{2}\right]\end{array}\right\} \tag{A.36}$$

$$I_{15}^{p}=\frac{\Theta_{11}}{60\left(R^{h}-R^{b}\right)^{2}}\begin{bmatrix}\left(R^{b}\right)^{5}\left(2R^{b}-3R^{h}\right)+15\left(R^{b}\right)\left(R^{h}\right)(R^{p})^{4}\\-12\left(R^{b}+R^{h}\right)(R^{p})^{5}+10(R^{p})^{6}\end{bmatrix} \tag{A.37}$$

$$I_{30}^{p}=I_{31}^{p}=\frac{\left(R^{b}\right)^{2}-(R^{p})^{2}}{4\left(R^{h}-R^{b}\right)^{2}}\Theta_{11} \tag{A.38}$$

$$I_{33}^{p}=\frac{\Theta_{12}}{120\left(R^{h}-R^{b}\right)^{2}}\left\{\begin{array}{c}10\left(R^{b}\right)^{6}-24\left(R^{b}\right)^{5}\left(R^{h}\right)+15\left(R^{b}\right)^{4}\left(R^{h}\right)^{2}\\+(R^{p})^{4}\left[-15\left(R^{h}\right)^{2}+24\left(R^{h}\right)(R^{p})-10(R^{p})^{2}\right]\end{array}\right\} \tag{A.39}$$

$$I_{34}^{p}=\frac{\left(R^{b}\right)^{2}-(R^{p})^{2}}{2\left(R^{h}-R^{b}\right)^{2}}\Theta_{11}=2I_{30}^{p} \tag{A.40}$$

$$I_{36}^{p}=\frac{\Theta_{61}}{30\left(R^{h}-R^{b}\right)^{2}}\left\{\begin{array}{c}\left(R^{b}\right)^{4}\left(3R^{b}-5R^{h}\right)+20\left(R^{b}\right)\left(R^{h}\right)(R^{p})^{3}\\-15\left(R^{b}+R^{h}\right)(R^{p})^{4}+12(R^{p})^{5}\end{array}\right\} \tag{A.41}$$

$$I_{38}^{p}=\frac{\Theta_{61}}{15\left(R^{h}-R^{b}\right)^{2}}\left\{\begin{array}{c}6\left(R^{b}\right)^{5}-15\left(R^{b}\right)^{4}\left(R^{h}\right)+10\left(R^{b}\right)^{3}\left(R^{h}\right)^{2}\\+(R^{p})^{3}\left[-10\left(R^{h}\right)^{2}+15\left(R^{h}\right)(R^{p})-6(R^{p})^{2}\right]\end{array}\right\} \tag{A.42}$$

$$J_{53}^{b}=J_{63}^{b}=\frac{\pi}{4}\left(R^{b}\right)^{4} \tag{A.43}$$

$$J_{40}^{a} = J_{41}^{a} = \frac{\pi\left[\left(R^{h}\right)^{2} - \left(R^{p}\right)^{2}\right]}{2\left(R^{h} - R^{b}\right)^{2}} \tag{A.44}$$

$$J_{44}^{a} = \frac{\pi\left[\left(R^{h}\right)^{2} - \left(R^{p}\right)^{2}\right]}{\left(R^{h} - R^{b}\right)^{2}} = 2J_{40}^{a} \tag{A.45}$$

$$J_{36}^{p} = J_{38}^{p} = \frac{2\left[\left(R^{b}\right)^{3} - \left(R^{p}\right)^{3}\right]}{9\left(R^{h} - R^{b}\right)^{2}}\Theta_{3} \tag{A.46}$$

$$J_{40}^{p} = J_{41}^{p} = \frac{\left(R^{b}\right)^{2} - \left(R^{p}\right)^{2}}{4\left(R^{h} - R^{b}\right)^{2}}\Theta_{12} \tag{A.47}$$

$$J_{44}^{p} = \frac{\left(R^{b}\right)^{2} - \left(R^{p}\right)^{2}}{2\left(R^{h} - R^{b}\right)^{2}}\Theta_{12} = 2J_{40}^{p} \tag{A.48}$$

$$J_{46}^{p} = J_{48}^{p} = -\frac{\left(R^{b}\right)^{3} - \left(R^{p}\right)^{3}}{9\left(R^{h} - R^{b}\right)^{2}}\Theta_{7} \tag{A.49}$$

$$J_{53}^{p} = \frac{\Theta_{12}}{120\left(R^{h} - R^{b}\right)^{2}}\left\{\begin{array}{l} 10\left(R^{b}\right)^{6} - 24\left(R^{b}\right)^{5}\left(R^{h}\right) + 15\left(R^{b}\right)^{4}\left(R^{h}\right)^{2} \\ +\left(R^{p}\right)^{4}\left[-15\left(R^{h}\right)^{2} + 24\left(R^{h}\right)\left(R^{p}\right) - 10\left(R^{p}\right)^{2}\right] \end{array}\right\} \tag{A.50}$$

$$J_{56}^{p} = -\frac{\Theta_{3}}{30\left(R^{h} - R^{b}\right)^{2}}\left[4\left(R^{b}\right)^{5} - 5\left(R^{b}\right)^{4}R^{h} + \left(5R^{h} - 4R^{p}\right)\left(R^{p}\right)^{4}\right] \tag{A.51}$$

$$J_{58}^{p} = \frac{\Theta_{61}}{15\left(R^{h} - R^{b}\right)^{2}}\left\{\begin{array}{l} 6\left(R^{b}\right)^{5} - 15\left(R^{b}\right)^{4}\left(R^{h}\right) + 10\left(R^{b}\right)^{3}\left(R^{h}\right)^{2} \\ +\left(R^{p}\right)^{3}\left[-10\left(R^{h}\right)^{2} + 15\left(R^{h}\right)\left(R^{p}\right) - 6\left(R^{p}\right)^{2}\right] \end{array}\right\} \tag{A.52}$$

$$J_{59}^{p} = \frac{\Theta_{61}}{60\left(R^{h} - R^{b}\right)^{2}}\left\{\begin{array}{l} -\left(R^{b}\right)^{3}\left[32\left(R^{b}\right)^{2} - 70\left(R^{b}\right)\left(R^{h}\right) + 40\left(R^{h}\right)^{2} + R^{b}\left(-4R^{b} + 5R^{h}\right)\Theta_{5}\right] \\ +\left(R^{p}\right)^{3}\left[40\left(R^{h}\right)^{2} - 70\left(R^{h}\right)\left(R^{p}\right) + 32\left(R^{p}\right)^{2} + \left(5R^{h} - 4R^{p}\right)R^{p}\Theta_{5}\right] \end{array}\right\} \tag{A.53}$$

$$J_{63}^{p} = \frac{\Theta_{11}}{120\left(R^{h} - R^{b}\right)^{2}}\left[\begin{array}{l} 10\left(R^{b}\right)^{6} - 24\left(R^{b}\right)^{5}\left(R^{h}\right) + 15\left(R^{b}\right)^{4}\left(R^{h}\right)^{2} \\ +\left(R^{p}\right)^{4}\left[-15\left(R^{h}\right)^{2} + 24\left(R^{h}\right)\left(R^{p}\right) - 10\left(R^{p}\right)^{2}\right] \end{array}\right] \tag{A.54}$$

$$J_{66}^{p} = J_{69}^{p} = -\frac{\Theta_{3}}{30\left(R^{h} - R^{b}\right)^{2}}\left[4\left(R^{b}\right)^{5} - 5\left(R^{b}\right)^{4}\left(R^{h}\right) + \left(5R^{h} - 4R^{p}\right)\left(R^{p}\right)^{4}\right] \tag{A.55}$$

$$\Theta_{0} = \sum_{n=1}^{N}\left(\theta_{1n} - \theta_{2n}\right) \tag{A.56}$$

$$\Theta_{11} = \sum_{n=1}^{N} (\theta_{1n} - \theta_{2n} - \sin\theta_{1n}\cos\theta_{1n} + \sin\theta_{2n}\cos\theta_{2n}) \tag{A.57}$$

$$\Theta_{12} = \sum_{n=1}^{N} (\theta_{1n} - \theta_{2n} + \sin\theta_{1n}\cos\theta_{1n} - \sin\theta_{2n}\cos\theta_{2n}) \tag{A.58}$$

$$\Theta_{21} = \sum_{n=1}^{N} (4\theta_{1n} - 4\theta_{2n} - \sin4\theta_{1n} + \sin4\theta_{2n}) \tag{A.59}$$

$$\Theta_{22} = \sum_{n=1}^{N} (4\theta_{1n} - 4\theta_{2n} + \sin4\theta_{1n} - \sin4\theta_{2n}) \tag{A.60}$$

$$\Theta_{3} = \sum_{n=1}^{N} \left(\sin^3\theta_{1n} - \sin^3\theta_{2n}\right) \tag{A.61}$$

$$\Theta_{4} = \sum_{n=1}^{N} [28(-\theta_{1n} + \theta_{2n}) + 16(\sin2\theta_{1n} - \sin2\theta_{2n}) - \sin4\theta_{1n} + \sin4\theta_{2n}] \tag{A.62}$$

$$\Theta_{5} = \sum_{n=1}^{N} (\cos2\theta_{1n} + \cos2\theta_{2n} - 2\sin\theta_{1n}\sin\theta_{2n}) \tag{A.63}$$

$$\Theta_{61} = \sum_{n=1}^{N} (\sin\theta_{1n} - \sin\theta_{2n}) \tag{A.64}$$

$$\Theta_{62} = \sum_{n=1}^{N} (\sin2\theta_{1n} - \sin2\theta_{2n}) \tag{A.65}$$

$$\Theta_{63} = \sum_{n=1}^{N} (\sin4\theta_{1n} - \sin4\theta_{2n}) \tag{A.66}$$

$$\Theta_{7} = \sum_{n=1}^{N} (3\sin\theta_{1n} + \sin3\theta_{1n} - 3\sin\theta_{2n} - \sin3\theta_{2n}) \tag{A.67}$$

$$\Theta_{8} = \sum_{n=1}^{N} (12\theta_{1n} - 12\theta_{2n} - 8\sin2\theta_{1n} + \sin4\theta_{1n} + 8\sin2\theta_{2n} - \sin4\theta_{2n}) \tag{A.68}$$

A.2 Components of mass and stiffness matrix and force vector

$$\begin{aligned} M_{fp}^{hbhb} = {} & \frac{2\rho^h I^h}{L} \int_{-1}^{1} \phi_p^{hb\prime} \phi_f^{hb\prime} d\xi + \frac{\rho^h A^h L}{2} \int_{-1}^{1} \phi_p^{hb} \phi_f^{hb} d\xi \\ & + \frac{2\rho^m (I_{10}^a + I_{10}^p)}{L^m} \int_{-1}^{1} \phi_p^{hb\prime} \phi_f^{hb\prime} d\xi^m + \frac{\rho^m (A_{30}^a + A_{30}^p) L^m}{2} \int_{-1}^{1} \phi_p^{hb} \phi_f^{hb} d\xi^m \end{aligned} \tag{A.69}$$

$$M_{fq}^{hbmb} = \frac{\rho^m (A_{34}^a + A_{34}^p) L^m}{4} \int_{-1}^{1} \phi_f^{hb} \phi_q^{mb} d\xi^m \tag{A.70}$$

$$M_{fr}^{hbms} = \frac{\rho^m (I_{15}^a + I_{15}^p)}{2} \int_{-1}^{1} \phi_f^{hb'} \phi_r^{ms} d\xi^m \tag{A.71}$$

$$M_{fs}^{hbmt} = \frac{\rho^m I_{36}^p L^m}{4} \int_{-1}^{1} \phi_f^{hb} \phi_s^{mt} d\xi^m \tag{A.72}$$

$$M_{gq}^{mbmb} = \frac{\rho^m \left(A_{31}^b + A_{31}^a + A_{31}^p\right) L^m}{2} \int_{-1}^{1} \phi_q^{mb} \phi_g^{mb} d\xi^m \tag{A.73}$$

$$M_{gr}^{mbms} = 0 \tag{A.74}$$

$$M_{gs}^{mbmt} = \frac{\rho^m I_{38}^p L^m}{4} \int_{-1}^{1} \phi_g^{mb} \phi_s^{mt} d\xi^m \tag{A.75}$$

$$M_{hr}^{msms} = \frac{\rho^m \left(I_{12}^b + I_{12}^a + I_{12}^p\right) L^m}{2} \int_{-1}^{1} \phi_r^{ms} \phi_h^{ms} d\xi^m \tag{A.76}$$

$$M_{hs}^{msmt} = 0 \tag{A.77}$$

$$M_{is}^{mtmt} = \frac{\rho^m \left(I_{23}^b + I_{33}^b + I_{23}^p + I_{33}^p\right) L^m}{2} \int_{-1}^{1} \phi_s^{mt} \phi_i^{mt} d\xi^m \tag{A.78}$$

$$\begin{aligned} K_{fp}^{hbhb} = {} & \frac{8\tilde{E}^h I^h}{L^3} \int_{-1}^{1} \phi_p^{hb''} \phi_f^{hb''} d\xi + \frac{8\tilde{E}^m \left(I_{10}^a + I_{10}^p\right)}{\left(L^m\right)^3} \int_{-1}^{1} \phi_p^{hb''} \phi_f^{hb''} d\xi^m \\ & + \frac{2\tilde{G}^m \left[k^a \left(A_{50}^a + A_{60}^a\right) + k^p \left(A_{50}^p + A_{60}^p\right)\right]}{L^m} \int_{-1}^{1} \phi_p^{hb'} \phi_f^{hb'} d\xi^m \\ & + \frac{\tilde{E}^m \left(I_{30}^a + I_{30}^p\right) L^m + \tilde{G}^m \left(k^a J_{40}^a + k^p J_{40}^p\right) L^m}{2} \int_{-1}^{1} \phi_p^{hb} \phi_f^{hb} d\xi^m \end{aligned} \tag{A.79}$$

$$\begin{aligned} K_{fq}^{hbmb} = {} & -\frac{\tilde{G}^m \left(k^a A_{54}^a + k^p A_{54}^p\right)}{L^m} \int_{-1}^{1} \phi_f^{hb'} \phi_q^{mb'} d\xi^m \\ & - \frac{\tilde{E}^m \left(I_{34}^a + I_{34}^p\right) L^m + \tilde{G}^m \left(k^a J_{44}^a + k^p J_{44}^p\right) L^m}{4} \int_{-1}^{1} \phi_q^{mb} \phi_f^{hb} d\xi^m \end{aligned} \tag{A.80}$$

$$\begin{aligned} K_{fr}^{hbms} = {} & \frac{2\tilde{E}^m \left(I_{15}^a + I_{15}^p\right)}{\left(L^m\right)^2} \int_{-1}^{1} \phi_f^{hb''} \phi_r^{ms'} d\xi^m \\ & - \frac{\tilde{G}^m \left[k^a \left(A_{55}^a + A_{65}^a\right) + k^p \left(A_{55}^p + A_{65}^p\right)\right]}{2} \int_{-1}^{1} \phi_f^{hb'} \phi_r^{ms} d\xi^m \end{aligned} \tag{A.81}$$

$$K_{fs}^{hbmt} = -\frac{\tilde{G}^m k^p \left(J_{56}^p - J_{66}^p\right)}{L^m} \int_{-1}^{1} \phi_f^{hb'} \phi_s^{mt'} d\xi^m - \frac{\left(\tilde{E}^m J_{36}^p - \tilde{G}^m k^p J_{46}^p\right) L^m}{4} \int_{-1}^{1} \phi_f^{hb} \phi_s^{mt} d\xi^m \tag{A.82}$$

$$\begin{aligned} K_{gq}^{mbmb} = {} & \frac{2\tilde{G}^m \left(k^b A_{51}^b + k^a A_{51}^a + k^p A_{51}^p\right)}{L^m} \int_{-1}^{1} \phi_q^{mb'} \phi_g^{mb'} d\xi^m \\ & + \frac{\tilde{E}^m \left(I_{31}^a + I_{31}^p\right) L^m + \tilde{G}^m \left(k^a J_{41}^a + k^p J_{41}^p\right) L^m}{2} \int_{-1}^{1} \phi_q^{mb} \phi_g^{mb} d\xi^m \end{aligned} \tag{A.83}$$

$$K_{gr}^{mbms} = -\frac{\tilde{G}^m \left(k^b A_{57}^b - k^a A_{57}^a - k^p A_{57}^p\right)}{2} \int_{-1}^{1} \phi_g^{mb\prime} \phi_r^{ms} d\xi^m \tag{A.84}$$

$$K_{gs}^{mbmt} = \frac{\tilde{G}^m k^p J_{58}^p}{L^m} \int_{-1}^{1} \phi_g^{mb\prime} \phi_s^{mt'} d\xi^m + \frac{\left(\tilde{E}^m J_{38}^p - \tilde{G}^m k^p J_{48}^p\right) L^m}{4} \int_{-1}^{1} \phi_g^{mb} \phi_s^{mt} d\xi^m \tag{A.85}$$

$$K_{hr}^{msms} = \frac{2\tilde{E}^m\left(I_{12}^b + I_{12}^a + I_{12}^p\right)}{L^m}\int_{-1}^{1}\phi_r^{ms\prime}\phi_h^{ms\prime}d\xi^m + \frac{\tilde{G}^m\left[k^b A_{52}^b + k^a\left(A_{52}^a + A_{62}^a\right) + k^p\left(A_{52}^p + A_{62}^p\right)\right]L^m}{2}\int_{-1}^{1}\phi_r^{ms}\phi_h^{ms}d\xi^m \tag{A.86}$$

$$K_{hs}^{msmt} = -\frac{\tilde{G}^m k^p\left(J_{69}^p - J_{59}^p\right)}{2}\int_{-1}^{1}\phi_h^{ms}\phi_s^{mt\prime}d\xi^m \tag{A.87}$$

$$K_{is}^{mtmt} = \frac{2\tilde{G}^m\left[k^b\left(J_{53}^b + J_{63}^b\right) + k^p\left(J_{53}^p + J_{63}^p\right)\right]}{L^m}\int_{-1}^{1}\phi_s^{mt\prime}\phi_i^{mt\prime}d\xi^m + \frac{\left[\tilde{E}^m\left(A_{23}^p + A_{33}^p\right) + \tilde{G}^m k^p A_{43}^p\right]L^m}{2}\int_{-1}^{1}\phi_s^{mt}\phi_i^{mt}d\xi^m \tag{A.88}$$

$$F_f^{hb} = \frac{L}{2}\int_{-1}^{1}F\phi_f^{hb}d\xi \tag{A.89}$$

References

[1] P.F. Pai, Metamaterial-based broadband elastic wave absorber, J. Intell. Mater. Syst. Struct. 21 (5) (2010) 517–528.
[2] H. Sun, X. Du, P.F. Pai, Theory of metamaterial beams for broadband vibration absorption, J. Intell. Mater. Syst. Struct. 21 (11) (2010) 1085–1101.
[3] P.F. Pai, H. Peng, S. Jiang, Acoustic metamaterial beams beased on multi-frequency vibration absorbers, Int. J. Mech. Sci. 79 (2014) 195–205.
[4] P. Wang, F. Casadei, S. Shan, J.C. Weaver, K. Bertoldi, Harnessing buckling to design tunable locally resonant acoustic metamaterials, Phys. Rev. Lett. 113 (2014) 014301.
[5] K.H. Matlack, A. Bauhofer, S. Krödel, A. Palermo, C. Daraio, Composite 3D-printed metastructures for low-frequency and broadband vibration absorption, Proc. Natl. Acad. Sci. 113 (30) (2016) 8386–8390.
[6] M. Nouh, O. Aldraihem, A. Baz, Wave propagation in metamaterial plates with periodic local resonances, J. Sound Vib. 341 (2015) 53–73.
[7] J.H. Oh, S. Qi, Y.Y. Kim, B. Assouar, Elastic metamaterial insulator for broadband low-frequency flexural vibration shielding, Phys. Rev. Appl 8 (5) (2017) 054034.
[8] X.N. Liu, G.K. Hu, C.T. Sun, G.L. Huang, Wave propagation characterization and design of two-dimensional elastic chiral metacomposite, J. Sound Vib. 330 (2011) 2536–2553.
[9] R. Zhu, X.N. Liu, G.K. Hu, C.T. Sun, G.L. Huang, A chiral elastic metamateiral beam for broadband vibration suppression, J. Sound Vib. 333 (2014) 2759–2773.
[10] E. Baravelli, M. Ruzzene, Internally resonating lattices for bandgap generation and low-frequency vibration control, J. Sound Vib. 332 (2013) 6562–6579.
[11] O. Abdeljaber, O. Avci, D.J. Inman, Optimization of chiral lattice based metastructures for broadband vibration suppression using genetic algorithms, J. Sound Vib. 369 (2016) 50–62.
[12] P. Aumjaud, C.W. Smith, K.E. Evans, A novel viscoelastic damping treatment for honeycomb sandwich structures, Compos. Struct. 119 (2015) 322–332.
[13] Y.C. Chen, S.C. Huang, An optimal placement of CLD treatment for vibration suppression of plates, Int. J. Mech. Sci. 44 (8) (2002) 1801–1821.
[14] J.L. Marcelin, P. Trompette, A. Smati, Optimal constrained layer damping with partial coverage, Finite Elem. Anal. Des. 12 (3–4) (1992) 273–280.
[15] H. Zheng, C. Cai, X.M. Tan, Optimization of partial constrained layer damping treatment for vibrational energy minimization of vibrating beams, Comput. Struct. 82 (29–30) (2004) 2493–2507.
[16] H. Zheng, C. Cai, G.S.H. Pau, G.R. Liu, Minimizing vibration response of cylindrical shells through layout optimization of passive constrained layer damping treatments, J. Sound Vib. 279 (739–756) (2005) 3–5.
[17] H. Zheng, G.S.H. Pau, Y.Y. Wang, A comparative study on optimization of constrained layer damping treatment for structural vibration control, Thin-Wall. Struct. 44 (8) (2006) 886–896.
[18] S.A. Nayfeh, Damping of flexural vibration in the plane of lamination of elastic–viscoelastic sandwich beams, J. Sound Vib. 276 (3–5) (2004) 689–711.
[19] J. Plattenburg, J.T. Dreyer, R. Singh, A new analytical model for vibration of a cylindrical shell and cardboard liner with focus on interfacial distributed damping, Mech. Syst. Sig. Process. 75 (2016) 176–195.
[20] J. Plattenburg, J.T. Dreyer, R. Singh, Vibration control of a cylindrical shell with concurrent active piezoelectric patches and passive cardboard liner, Mech. Syst. Sig. Process. 91 (2017) 422–437.
[21] B.E. Douglas, J.C.S. Yang, Transverse compressional damping in the vibratory response of elastic-viscoelastic-elastic beams, AIAA J. 16 (9) (1978) 925–930.
[22] E.M. Kerwin Jr., Damping of flexural waves by a constrained viscoelastic layer, J. Acoust. Soc. Am. 31 (7) (1959) 952–962.
[23] J. Bishop, Q. Dai, Y. Song, R.L. Harne, Resilience to impact by extreme energy absorption in lightweight material inclusions constrained near a critical point, Adv. Eng. Mater. 18 (2016) 1871–1876.
[24] R.L. Harne, Y. Song, Q. Dai, Trapping and attenuating broadband vibroacoustic energy with hyperdamping metamaterials, Extreme Mech. Lett. 12 (2017) 41–47.
[25] O. Beslin, J. Nicolas, A hierarchical functions set for predicting very high order plate bending modes with any boundary conditions, J. Sound Vib. 202 (5) (1997) 633–655.
[26] L. Dozio, On the use of the trigonometric Ritz method for general vibration analysis of rectangular Kirchhoff plates, Thin-Wall. Struct. 49 (1) (2011) 129–144.
[27] J.E. Ruzicka, Damping structural resonances using viscoelastic shear-damping mechanisms, part i: design configurations, J. Eng. Ind. 83 (1961) 403–413.
[28] P.J. Torvik, The analysis and design of constrained layer damping treatments, Air Force Institute of Technology Wright-Patterson AFB, Ohio, USA, 1980 (Technical Report AFIT TR 80-4).
[29] G.R. Cowper, The shear coefficient in Timoshenko's beam theory, J. Appl. Mech. 33 (2) (1966) 335–340.
[30] S.S. Rao, Vibration of Continuous Systems, John Wiley & Sons Inc, Hoboken, New Jersey, 2007.

[31] C.G. Cooley, T.Q. Tran, T. Chai, Comparison of viscous and structural damping models for piezoelectric vibration energy harvesters, Mech. Syst. Sig. Process. 110 (2018) 130–138.
[32] N. Kumar, S.P. Singh, Vibration control of curved panel using smart damping, Mech. Syst. Sig. Process. 30 (2012) 232–247.